The Astrophysical Journal, 893:1 (23pp), 2020 April 10 https://doi.org/10.3847/1538-4357/ab7ea9


# A Comparison of UV and Optical Metallicities in Star-forming Galaxies

Nell Byler[1,2], Lisa J. Kewley[1,2], Jane R. Rigby[3], Ayan Acharyya[1,2], Danielle A. Berg[4,5], Matthew Bayliss[6], and Keren Sharon[7]

[1] Research School of Astronomy and Astrophysics, The Australian National University, ACT, Australia; nell.byler@anu.edu.au
[2] ARC Centre of Excellence for All Sky Astrophysics in 3 Dimensions (ASTRO 3D), Australia
[3] Observational Cosmology Lab, NASA Goddard Space Flight Center, 8800 Greenbelt Road, Greenbelt, MD 20771, USA
[4] Center for Gravitation, Cosmology and Astrophysics, Department of Physics, University of Wisconsin Milwaukee, 1900 East Kenwood Boulevard, Milwaukee, WI 53211, USA
[5] Department of Astronomy, The Ohio State University, 140 W. 18th Avenue, Columbus, OH 43202, USA
[6] MIT Kavli Institute for Astrophysics and Space Research, 77 Massachusetts Avenue, Cambridge, MA 02139, USA
[7] Department of Astronomy, University of Michigan, 1085 South University Avenue, Ann Arbor, MI 48109, USA
*Received 2019 September 6; revised 2020 March 8; accepted 2020 March 9; published 2020 April 8*

## Abstract

Our ability to study the properties of the interstellar medium in the earliest galaxies will rely on emission-line diagnostics at rest-frame ultraviolet (UV) wavelengths. In this work, we identify metallicity-sensitive diagnostics using UV emission lines. We compare UV-derived metallicities with standard, well-established optical metallicities using a sample of galaxies with rest-frame UV and optical spectroscopy. We find that the He2–O3C3 diagnostic (He II $\lambda$1640 Å/C III] $\lambda$1906,1909 Å versus [O III] $\lambda$1666 Å/C III] $\lambda$1906,9 Å) is a reliable metallicity tracer, particularly at low metallicity ($12 + \log_{10}(\mathrm{O/H}) \leqslant 8$), where stellar contributions are minimal. We find that the Si3–O3C3 diagnostic ([Si III] $\lambda$1883 Å/C III] $\lambda$1906 Å versus [O III] $\lambda$1666 Å/C III] $\lambda$1906,9 Å) is a reliable metallicity tracer, though with large scatter (0.2–0.3 dex), which we suggest is driven by variations in gas-phase abundances. We find that the C4–O3C3 diagnostic (C IV $\lambda$ 1548,50 Å/[O III] $\lambda$ 1666 Å versus [O III] $\lambda$ 1666 Å/C III] $\lambda$ 1906,9 Å) correlates poorly with optically derived metallicities. We discuss possible explanations for these discrepant metallicity determinations, including the hardness of the ionizing spectrum, contribution from stellar wind emission, and non-solar-scaled gas-phase abundances. Finally, we provide two new UV oxygen abundance diagnostics, calculated from polynomial fits to the model grid surface in the He2–O3C3 and Si3–O3C3 diagrams.

*Unified Astronomy Thesaurus concepts:* Metallicity (1031); Ultraviolet astronomy (1736); Emission line galaxies (459); Galaxy abundances (574); Massive stars (732)

## 1. Introduction

Quantifying the buildup of stellar mass and metals in galaxies over cosmic time is critical in understanding how galaxies form and evolve. Changes in mass and metallicity are intertwined through the star formation process, as gas is converted into stars and subsequently enriched within stars through nucleosynthetic processes. Some of this enriched gas is eventually expelled via stellar winds or supernovae (SNe), and thereby returned to the interstellar medium (ISM). As star formation continues and this enrichment process repeats, the metal content of the galaxy increases (e.g., Nomoto et al. 2013).

The specific pattern of elemental abundances in a given galaxy depends on the history of star formation (Pagel & Tautvaisiene 1995). In turn, the duration and efficiency of star formation depend on both the availability of gas and its ability to collapse and form stars. For a given gas cloud, the balance between gravity and thermal pressure is mediated by the temperature, density, and chemical composition of the gas itself (Evans 1999). Thus, understanding the mechanisms that drive and sustain star formation relies on our ability to measure the physical properties of the ISM (see recent reviews by Peimbert et al. 2017; Maiolino & Mannucci 2018; Kewley et al. 2019b; and references therein).

Fortunately, emission from ionized gas (nebular emission) in galaxies is easily observable via bright emission lines such as the hydrogen recombination transitions (e.g., H$\alpha$) and the radiative de-excitation of collisionally excited metal ions (e.g., [O III] $\lambda$ 5007). These emission lines encode information about dust attenuation and the local gas conditions, including the temperature, chemical composition, density, and ionization state of the gas. We can extract the properties of the ISM by comparing the relative strengths of various emission lines with predictions from atomic physics (e.g., Sargent & Searle 1970; Searle & Sargent 1972; McKee & Ostriker 1977; Pagel et al. 1979; McGaugh 1991; Zaritsky et al. 1994; Kewley & Dopita 2002; Pilyugin & Thuan 2005; Berg et al. 2015).

Ratios of emission lines that have proven to be particularly sensitive to properties like metallicity or density are called "emission-line diagnostics." The best-known emission-line diagnostics use transitions at optical wavelengths. There is a long history of using these emission-line diagnostics to constrain the physical properties of the ISM in galaxies with redshifts between $0 < z < 4$ (e.g., Tremonti et al. 2004; Erb et al. 2006; Brinchmann et al. 2008; Shapley 2011; Steidel et al. 2014; Zahid et al. 2014; Bian et al. 2017, and many others).

However, for observations of distant galaxies ($z \gtrsim 4$), these well-established optical emission-line diagnostics become inaccessible to ground-based optical and infrared facilities, as the expansion of the universe redshifts these lines out of observational windows. To probe the physical conditions of the gas in the earliest galaxies, we must instead rely on emission-line diagnostics that originate in the rest-frame ultraviolet (UV) part of the spectrum. Many studies have identified promising

emission lines in the UV that can be used to probe ISM conditions in the most distant galaxies (e.g., Kinney et al. 1993; Garnett et al. 1995; Heckman et al. 1998; Shapley et al. 2003; Leitherer et al. 2011; Bayliss et al. 2014; James et al. 2014; Stark et al. 2014; Zetterlund et al. 2015; Feltre et al. 2016; Steidel et al. 2016; Du et al. 2017; Byler et al. 2018).

Unfortunately, the properties of both nebular and stellar emission in the UV are still poorly understood, driven by our comparative lack of UV spectroscopy. UV photons are more difficult to detect than in the optical and generally require space-based observatories. Moreover, observations of star-forming galaxies in the rest-frame UV have revealed complex and overlapping features, including broad emission features (e.g., He II $\lambda$1640 Å; Leitherer et al. 2018), emission associated with stellar winds (C IV $\lambda$1550, Si IV $\lambda$1400 Å; Pettini et al. 2000, also Chisholm et al. 2019), and emission from resonant transitions or transitions with a nonstellar ionization source (e.g., continuum upscattering in Mg II $\lambda$2796 Å; Rigby et al. 2014). In many cases, these nonnebular features overlap with nebular emission lines. Line profiles can be further complicated by interstellar absorption features, making the interpretation of UV emission lines challenging (Vidal-García et al. 2017).

Overcoming these challenges is crucial for studying the most distant galaxies. Future surveys using the multiobject Near Infrared Spectrograph (NIRSpec) on the James Webb Space Telescope (JWST) will provide rest-UV spectra for thousands of galaxies at redshifts above $z \sim 5$. The Mid-Infrared Instrument (MIRI) on JWST extends to longer wavelengths, 5–30 $\mu$m, compared to the 0.6–5 $\mu$m covered by NIRSpec. However, MIRI is not multiplexed, and it will be impossible to obtain rest-optical spectroscopy for most of the galaxies observed with NIRSpec. Similar challenges exist for ground-based spectra: 30 m class telescopes will observe the rest-UV for distant galaxies in the infrared, but Earth's atmosphere makes it impossible to obtain the rest-optical at far-infrared wavelengths. Thus, our most cost-effective means of understanding the gas in these objects will come from their rest-UV emission.

Before UV emission-line diagnostics can be applied to large samples of high-redshift galaxies, we must test whether or not the diagnostics can accurately recover key astrophysical parameters like the gas-phase metallicity. Moreover, to robustly compare the properties of high-redshift galaxies with the results from lower redshift studies, we must first establish that predictions from UV emission-line diagnostics are consistent with predictions from optical emission-line diagnostics. However, calibrating UV and optical emission-line diagnostics is a nontrivial task for two reasons. First, the task requires a sample of star-forming galaxies with rest-UV and rest-optical emission-line spectroscopy. Second, to properly study the evolution of ISM properties over cosmic time, the sample should span a range of redshifts, so that metallicity calibrations are not biased to local ISM conditions.

In recent years, significant effort has gone into compiling samples of galaxies with rest-UV and rest-optical spectroscopy. Berg et al. (2016, 2019) and Senchyna et al. (2017, 2019) used the Hubble Space Telescope (HST) Cosmic Origins Spectrograph (COS) to obtain UV spectroscopy for nearby galaxies that already have optical spectroscopy from SDSS. Samples are still small (26 and 16 objects, respectively), because it is difficult to predict the signal-to-noise ratio (S/N) of UV emission lines without preliminary UV spectra.

Above $z \gtrsim 1$, the rest-frame UV is redshifted into the observed optical and infrared, wavelength ranges that are accessible from ground-based telescopes. However, the improved observational access comes at the expense of detectability, as distant galaxies are, in general, fainter. Thus, rest-frame UV spectroscopic surveys of high-redshift objects have generally taken three approaches: (1) probe extreme objects with emission-line fluxes high enough for direct detection (e.g., Erb et al. 2010; Stark et al. 2014), (2) target galaxies that have been magnified via gravitational lensing (e.g., Bayliss et al. 2014; Rigby et al. 2018b), or (3) create composite spectra from stacks of individual galaxy spectra (e.g., Shapley et al. 2003; Steidel et al. 2016). The calibration of UV metallicity diagnostics should be based on spectra from individual galaxies because stacking can be influenced by outliers, and we thus focus on objects from the first two approaches. However, both approaches rely on relatively rare objects and samples are small (of order 10 galaxies).

In this work, we test the UV emission-line diagnostics presented in Byler et al. (2018) using a sample of local galaxies ($z < 0.1$) and moderate-redshift galaxies ($z = 2$–$3$) with rest-frame UV and optical spectra. We first calculate metallicities using UV emission lines. We then compare the metallicities calculated from UV emission lines with metallicities calculated from optical emission lines to identify which UV diagnostics are most consistent with optical diagnostics. For future studies where only rest-frame UV spectroscopy is available, this comparison provides a crucial link between abundances derived using UV emission lines and optical emission lines.

The structure of the paper is as follows. We describe the stellar and nebular model in Sections 2.1 and 2.2, respectively. We introduce the sample in Section 3, including local galaxies (Section 3.1) and moderate-redshift galaxies (Section 3.2) with rest-UV and rest-optical spectra. We discuss abundance determinations in Section 4. We determine theoretical abundance calibrations in Section 4.1 and calculate UV-based metallicities for the comparison samples in Section 4.2. We compare UV and optical abundance metallicities in Section 5. In Section 6, we discuss problematic UV metallicity diagnostics and sources of significant uncertainty, including the contribution from stellar wind emission, and the use of rotating and binary star models. Finally, we summarize our conclusions in Section 7.

## 2. Description of Model

The stellar and nebular models are described at length in Byler et al. (2018; hereafter B18); we briefly summarize the most relevant information here.

### 2.1. Stellar Model

For stellar population synthesis, we use the Flexible Stellar Population Synthesis package (FSPS; Conroy et al. 2009; Conroy & Gunn 2010) via the Python interface, **`python-fsps`** (Foreman-Mackey et al. 2014).[8]

We use the MESA Isochrones & Stellar Tracks (MIST; Choi et al. 2016; Dotter 2016), single-star stellar evolutionary models which include the effect of stellar rotation. The evolutionary tracks are computed using the publicly available stellar evolution package Modules for Experiments in Stellar

[8] GitHub commit hash `d1bb5d5`.

**Table 1**
Population Synthesis Model Parameters

| Stellar Model | Hot Star Spectral Libraries | IMF | SFH |
|---|---|---|---|
| MIST | WM-basic (O- and B-type stars; Eldridge et al. 2017)<br>CMFGEN (W-R stars; Hillier & Lanz 2001) | Kroupa (2001);<br>$M_{\rm lower} = 0.08\ M_{\odot}$,<br>$M_{\rm upper} = 120\ M_{\odot}$. | Constant SFR |
| BPASS | WM-basic (O- and B-type stars; Eldridge et al. 2017)<br>PoWR (W-R stars; Hamann & Gräfener 2003) | Kroupa (2001);<br>$M_{\rm lower} = 0.08\ M_{\odot}$,<br>$M_{\rm upper} = 120\ M_{\odot}$. | Constant SFR |

Astrophysics (MESA v7503; Paxton et al. 2011, 2013, 2015). The MIST models cover ages from $10^5$ to $10^{10.3}$ yr, initial masses from 0.1 to 300 $M_{\odot}$, and metallicities between $-2.0 \leqslant [Z/{\rm H}] \leqslant 0.5$ in steps of 0.25 dex. MIST adopts the protosolar abundances recommended by Asplund et al. (2009) as the reference scale for all metallicities, such that $[Z/{\rm H}]$ is computed with respect to $Z = Z_{\odot,{\rm protosolar}} = 0.0142$ rather than $Z = Z_{\odot,{\rm photosphere}} = 0.0134$, the present-day photospheric abundances.

We combine the MIST tracks with a high-resolution theoretical spectral library (C3K; C. Conroy et al. 2020, in preparation) based on Kurucz stellar atmosphere and spectral synthesis routines (ATLAS12 and SYNTHE; Kurucz 2005). The C3K library is supplemented with alternative spectral libraries for very hot stars and stars in rapidly evolving evolutionary phases. For main-sequence stars with temperatures above 25,000 K (O- and B-type stars), we use WM-basic (Pauldrach et al. 2001) spectra, as described in Eldridge et al. (2017). For Wolf–Rayet (W-R) stars, we use the spectral library from Smith et al. (2002), computed using CMFGEN (Hillier & Lanz 2001).

We note that even though the stellar masses in the MIST models extend to 300 $M_{\odot}$, we adopt a Kroupa initial mass function (IMF; Kroupa 2001) with an upper and lower mass limit of 120 $M_{\odot}$ and 0.08 $M_{\odot}$, respectively.

In Section 6, we consider the effect of binary stars. FSPS includes precomputed simple stellar populations (SSPs) from the Binary Population and Spectral Synthesis code (BPASS, v2.2; Eldridge et al. 2017). All population synthesis parameters are summarized in Table 1.

### 2.2. Nebular Model

We use the nebular model implemented within FSPS, **`CloudyFSPS`** (Byler 2018), to generate spectra that include nebular line and nebular continuum emission. Calculations were performed with the photoionization code Cloudy (v13.03; Ferland et al. 2013).

The nebular model is a grid in (1) SSP age, (2) SSP and gas-phase metallicity, and (3) ionization parameter, $\mathcal{U}_0$, a dimensionless quantity that gives the ratio of ionizing photons to the total hydrogen density. We use the Cloudy definition of $\mathcal{U}_0$, which is computed at the illuminated inner face of the gas cloud.

The model uses FSPS to generate single-age, single-metallicity stellar populations. Using the photoionization code Cloudy, the SSP is used as the ionization source for the gas cloud and the gas-phase metallicity is scaled to the metallicity of the SSP. For each SSP of age $t$ and metallicity $Z$, photoionization models are run at different ionization parameters, $\mathcal{U}_0$, from $\log_{10}\mathcal{U}_0 = -4$ to $\log_{10}\mathcal{U}_0 = -1$ in steps of 0.5 dex. $\mathcal{U}_0$ is a free parameter, but the nebular line fluxes are scaled to the ionizing photon flux of the input spectrum. For a detailed discussion of this intensity scaling, see Section 2.1.4 of Byler et al. (2017).

Star clusters do not form instantaneously and may be better modeled by a population with a range of ages spanning a few million years. To account for more extended, complex star formation histories (SFHs), we also generate stellar populations assuming a continuous star formation rate (CSFR). For continuous star formation models, the rate of stars forming and the rate of stars evolving off the main sequence eventually reaches an equilibrium. As noted in B18, the MIST models with continuous star formation reach a "steady state" between 7 and 10 Myr, after which the ionizing properties change very little.

A full comparison of the instantaneous burst and CSFR models can be found in B18. In what follows, we assume stellar populations with continuous star formation over 10 Myr (1 $M_{\odot}$ yr$^{-1}$). We note that the use of CSFR models may not be appropriate for massive H II regions and galaxies with extremely bursty SFHs.

Reported emission-line strengths always reflect the pure nebular emission-line intensities. However, in Sections 6.2–6.4, we discuss possible contamination from stellar emission.

#### 2.2.1. Gas-phase Abundances

The abundances used in this work follow those used in B18. We assume that the gas-phase metallicity scales with the metallicity of the stellar population (i.e., $Z_{\rm gas} \approx Z_{\rm stars}$), given that the metallicity of the most massive stars should be identical to the metallicity of the gas cloud from which the stars formed. Both the gas-phase and stellar abundances are solar-scaled, such that that individual elemental abundances are monolithically scaled up or down with metallicity, $[Z/{\rm H}]$. In practice, $[Z/{\rm H}]$ scales with $[{\rm Fe/H}]$ for the stellar models and with $[{\rm O/H}]$ for the gas-phase abundances.

In this work, we use models with stellar metallicities between $-2.0 \leqslant [{\rm Fe/H}] \leqslant 0.25$ in steps of 0.25 dex, which corresponds to gas-phase oxygen abundances between $6.69 \leqslant 12 + \log_{10}({\rm O/H}) \leqslant 8.94$ in steps of 0.25 dex. In what follows, we often use the terms gas-phase metallicity and oxygen abundance interchangeably, because these quantities scale equivalently in our model.

For most elements, we use the solar abundances from Grevesse et al. (2010), based on the results from Asplund et al. (2009), and adopt the dust depletion factors specified by Dopita et al. (2013). The abundance for each element and dust depletion factors at solar metallicity are given in Table 2. Notably, there are a few elements (C, N) with gas-phase abundances that deviate from perfect solar scaling, due to additional production mechanisms that operate at high

**Table 2**
Elemental Abundances and Adopted Depletion Factors $D$ for Each Element in the Nebular Model at Solar Metallicity, Which Has $Z = 0.0142$ ($\log_{10}(\mathrm{O/H}) = -3.31$ or $12 + \log_{10}(\mathrm{O/H}) = 8.69$)

| Element | $\log_{10}(E/\mathrm{H})$ | $\log_{10}(D)$ |
|---|---|---|
| H | 0 | 0 |
| He | −1.01 | 0 |
| C | −3.57 | −0.30 |
| N | −4.60 | −0.05 |
| O | −3.31 | −0.07 |
| Ne | −4.07 | 0 |
| Na | −5.75 | −1.00 |
| Mg | −4.40 | −1.08 |
| Al | −5.55 | −1.39 |
| Si | −4.49 | −0.81 |
| S | −4.86 | 0 |
| Cl | −6.63 | −1.00 |
| Ar | −5.60 | 0 |
| Ca | −5.66 | −2.52 |
| Fe | −4.50 | −1.31 |
| Ni | −5.78 | −2.00 |

**Note.** Solar abundances are from Grevesse et al. (2010) and depletion factors are from Dopita et al. (2013).

metallicity (secondary or pseudo-secondary nucleosynthetic production; for details, see Berg et al. 2016). We describe the scaling for these elements below.

To set the relationship between N/H and O/H, we use the following equation from B18:

$$\log_{10}(\mathrm{N/O}) = -1.5 + \log\left(1 + e^{\frac{12+\log_{10}(\mathrm{O/H})-8.3}{0.1}}\right), \quad (1)$$

and for C/H and O/H:

$$\log_{10}(\mathrm{C/O}) = -0.8 + 0.14 \cdot (12 + \log_{10}(\mathrm{O/H}) - 8.0) + \log\left(1 + e^{\frac{12+\log_{10}(\mathrm{O/H})-8.0}{0.2}}\right). \quad (2)$$

The relationships from B18 for N/H and C/H with O/H were modified from the empirically calculated Dopita et al. (2013) relationships to better match observations below $12 + \log_{10}(\mathrm{O/H}) = 8$, which did not exist when the original relationships were published. For $12 + \log_{10}(\mathrm{O/H}) = 8.69$ (solar metallicity), this corresponds to $\log_{10}(\mathrm{N/O}) = -1.09$ and $\log_{10}(\mathrm{C/O}) = -0.26$, including the effects of dust depletion, typical of star-forming galaxies with $12 + \log\mathrm{O/H} = 8.7$ (e.g., Belfiore et al. 2017). For a more complete discussion of N/O and C/O ratios used in photoionization models, we refer the reader to Appendix B of B18. We note that empirically derived relationships are always limited by the calibration sample, and detailed gas-phase abundance studies are only feasible in the local universe. As such, these locally derived relations may not be appropriate for high-redshift systems.

*C/O variations*—The C III] λ1906,1909 emission lines are the brightest UV emission lines after Lyα. As such, the C III] lines are optimal candidates for emission-line diagnostics. However, it has not yet been established whether or not these lines provide a robust tracer for the gas-phase oxygen abundance. Observed C/O ratios vary by more than 0.6 dex between $7 \lesssim 12 + \log_{10}(\mathrm{O/H}) \lesssim 8$ (Berg et al. 2019). Using detailed chemical evolution models, Berg et al. (2019) found that the C/O ratio is sensitive to both the detailed SFH and supernova feedback. This implies that the UV C III] and oxygen emission lines *alone* may not provide a reliable indicator of the gas-phase oxygen abundance. Robust metallicity diagnostics may require additional spectral features.

*Decoupled stellar and gas-phase abundances*—Recent work has suggested decoupling the stellar metallicity from the gas-phase metallicity to approximate scenarios in which high star formation rates rapidly enrich the gas in α-elements (e.g., Steidel et al. 2016). In practice, this involves pairing gas of a given oxygen abundance with a slightly more metal-poor (i.e., lower iron abundance) stellar ionizing spectrum. This ultimately increases the excitation of the nebula, because ionizing spectra are harder with decreasing metallicity. Observationally, the prevalence and scale of this α-enrichment have yet to be determined. Recent work by Senchyna et al. (2019) compared stellar iron abundances and gas-phase oxygen abundances in nearby galaxies based on UV spectra and did not find significantly α-enhanced gas.

## 3. Data

We compare our models to two observational samples: (1) nearby star-forming galaxies ($z < 0.04$) with UV and optical spectroscopy, and (2) moderate-redshift star-forming galaxies ($z \gtrsim 1.5$) with optical and near-infrared (NIR) spectroscopy that probes rest-frame UV and optical wavelengths. References for all galaxies used in the sample can be found in Table 3. We briefly describe the two samples below.

### 3.1. Local Blue Compact Dwarf Galaxies

Berg et al. (2016) presented UV and optical spectra for a sample of seven nearby, low-metallicity, high-ionization blue compact dwarf galaxies (BCDs). We include 19 additional galaxies from Berg et al. (2019); the combined sample of 26 galaxies is hereafter referred to as the Berg sample. The galaxies are nearby ($0.003 < z < 0.040$), UV bright ($m_{\mathrm{FUV}} \leqslant 19.5$ AB), compact ($D < 5''$), low metallicity ($7.2 \leqslant 12 + \log_{10}(\mathrm{O/H}) \leqslant 8.0$), and low extinction ($0.05 < E(B-V) < 0.2$. These galaxies have relatively low masses ($\sim 10^7\,M_\odot$) and high specific star formation rates (sSFRs; $\sim 10^{-8}\,\mathrm{yr}^{-1}$).

We use the dereddened UV emission-line fluxes and optical oxygen abundances published in Berg et al. (2016, 2019). All of the galaxies in the sample have auroral line detections for direct-method calculations of the nebular temperature, density, and metallicity. The UV spectra were obtained with HST COS using the G140L grating and cover roughly 1300–2000 Å. This wavelength coverage includes a number of emission lines, including C IV λ 1548,1551, He II λ 1640, [O III] λ1661,1666, [Si III] λ1883,1892, and C III] λ1906,1909.[9]

*Other local BCD observations*—Where possible, we also compare our models to the sample of local BCDs from Senchyna et al. (2017, 2019), which have similar properties to the Berg et al. (2016) galaxies and were also observed with HST COS. However, the Senchyna et al. (2017) observations used the G185M and G160M gratings, which provide increased spectral resolution at the expense of wavelength coverage. As a result, the Senchyna et al. (2017) BCD sample has fewer emission lines observed than the Berg et al. (2016) sample, but the higher spectral resolution (typical FWHM of 0.6 Å,

[9] For convenience, in this work C III] λ1906,1909 represents the combination of the forbidden [C III] λ1906 line and the semi-forbidden C III] λ1909 line.

**Table 3**
Literature (Optical) and Derived (UV) Gas-phase Oxygen Abundances

| References | Object | Optical Abundance | | UV $12 + \log_{10}(O/H)$ Abundance | | |
|---|---|---|---|---|---|---|
| | | $12 + \log_{10}(O/H)$ | Method | Si3–O3C3 | He2–O3C3 | C4–O3C3 |
| (1) | J223831 | $7.59 \pm 0.02$ | direct | $8.05^{+0.31}_{-0.15}$ | ⋯ | $8.93^{+0.26}_{-0.50}$ |
| (1) | J141851 | $7.54 \pm 0.02$ | direct | $8.00^{+0.05}_{-0.14}$ | $7.59^{+0.07}_{-0.08}$ | $7.99^{+0.09}_{-0.08}$ |
| (1) | J120202 | $7.63 \pm 0.02$ | direct | $8.05^{+0.15}_{-0.17}$ | $7.97^{+0.11}_{-0.24}$ | ⋯ |
| (1) | J121402 | $7.67 \pm 0.02$ | direct | $8.21^{+0.18}_{-0.13}$ | ⋯ | $8.49^{+0.09}_{-0.39}$ |
| (1) | J084236 | $7.61 \pm 0.02$ | direct | ⋯ | ⋯ | $7.94^{+0.50}_{-0.66}$ |
| (1) | J171236 | $7.70 \pm 0.02$ | direct | $7.55^{+0.72}_{-0.38}$ | $7.87^{+0.16}_{-0.09}$ | $8.72^{+0.23}_{-0.46}$ |
| (1) | J113116 | $7.65 \pm 0.02$ | direct | ⋯ | $7.76^{+0.19}_{-0.19}$ | $8.19^{+0.25}_{-0.55}$ |
| (1) | J133126 | $7.69 \pm 0.02$ | direct | $8.07^{+0.17}_{-0.11}$ | $7.91^{+0.09}_{-0.06}$ | ⋯ |
| (1) | J132853 | $7.73 \pm 0.02$ | direct | ⋯ | ⋯ | ⋯ |
| (1) | J095430 | $7.70 \pm 0.02$ | direct | $8.08^{+0.26}_{-0.13}$ | $7.95^{+0.06}_{-0.09}$ | $8.38^{+0.15}_{-0.38}$ |
| (1) | J132347 | $7.58 \pm 0.02$ | direct | $7.63^{+0.59}_{-0.20}$ | $7.45^{+0.09}_{-0.10}$ | $8.19^{+0.36}_{-0.36}$ |
| (1) | J094718 | $7.73 \pm 0.02$ | direct | $8.23^{+0.16}_{-0.10}$ | ⋯ | $8.92^{+0.21}_{-0.19}$ |
| (1) | J150934 | $7.71 \pm 0.02$ | direct | $8.04^{+0.37}_{-0.20}$ | $7.86^{+0.15}_{-0.11}$ | $8.11^{+0.13}_{-0.18}$ |
| (1) | J100348 | $7.74 \pm 0.02$ | direct | $8.27^{+0.82}_{-0.25}$ | ⋯ | $8.36^{+0.17}_{-0.18}$ |
| (1) | J025346 | $7.91 \pm 0.02$ | direct | $7.86^{+0.42}_{-0.27}$ | ⋯ | $8.42^{+0.11}_{-0.19}$ |
| (1) | J015809 | $7.75 \pm 0.02$ | direct | $8.14^{+0.65}_{-0.21}$ | ⋯ | $8.44^{+0.19}_{-0.18}$ |
| (1) | J104654 | $7.91 \pm 0.02$ | direct | $8.16^{+0.22}_{-0.05}$ | ⋯ | ⋯ |
| (1) | J093006 | $8.02 \pm 0.02$ | direct | ⋯ | ⋯ | ⋯ |
| (1) | J092055 | $7.87 \pm 0.02$ | direct | $7.77^{+0.36}_{-0.24}$ | $7.95^{+0.07}_{-0.08}$ | $8.29^{+0.10}_{-0.09}$ |
| (1) | J082555 | $7.37 \pm 0.01$ | direct | $8.16^{+0.03}_{-0.02}$ | $8.09^{+0.02}_{-0.02}$ | $8.27^{+0.02}_{-0.02}$ |
| (1) | J104457 | $7.45 \pm 0.02$ | direct | $8.02^{+0.03}_{-0.03}$ | $7.74^{+0.03}_{-0.03}$ | $7.94^{+0.00}_{-0.00}$ |
| (1) | J120122 | $7.45 \pm 0.03$ | direct | ⋯ | ⋯ | ⋯ |
| (1) | J124159 | $7.73 \pm 0.04$ | direct | $7.97^{+0.11}_{-0.09}$ | ⋯ | ⋯ |
| (1) | J122622 | $7.90 \pm 0.01$ | direct | ⋯ | ⋯ | ⋯ |
| (1) | J122436 | $7.84 \pm 0.02$ | direct | ⋯ | ⋯ | ⋯ |
| (1) | J124827 | $7.81 \pm 0.03$ | direct | ⋯ | $7.72^{+0.09}_{-0.10}$ | $8.67^{+0.20}_{-0.46}$ |
| (2) | rcs0327-B | $8.11 \pm 0.10$ | PP04-N2 | $8.17^{+0.20}_{-0.08}$ | $7.57^{+0.07}_{-0.07}$ | ⋯ |
| (2) | rcs0327-E | $8.40 \pm 0.10$ | PP04-N2 | $8.30^{+0.01}_{-0.11}$ | $7.86^{+0.07}_{-0.06}$ | ⋯ |
| (2) | rcs0327-G | ⋯ | ⋯ | $8.17^{+0.12}_{-0.07}$ | $7.91^{+0.09}_{-0.04}$ | ⋯ |
| (2) | rcs0327-U | $8.16 \pm 0.10$ | PP04-N2 | ⋯ | ⋯ | ⋯ |
| (2) | S0004-0103 | $\leqslant 8.10$ | PP04-N2 | $7.99^{+0.51}_{-0.21}$ | $7.58^{+0.13}_{-0.15}$ | ⋯ |
| (2) | S0108+0624 | ⋯ | ⋯ | ⋯ | ⋯ | ⋯ |
| (2) | S0900+2234 | $8.12 \pm 0.10$ | PP04-N2 | ⋯ | ⋯ | ⋯ |
| (2) | S0957+0509 | ⋯ | ⋯ | $8.03^{+0.08}_{-0.08}$ | $7.82^{+0.09}_{-0.08}$ | ⋯ |
| (2) | Cosmic Horseshoe | $8.45 \pm 0.10$ | PP04-N2 | ⋯ | ⋯ | ⋯ |
| (2) | S1226+2152 | $7.89 \pm 0.30$ | KK04-R23-l | ⋯ | ⋯ | ⋯ |
| (2) | S1429+1202 | ⋯ | ⋯ | ⋯ | $6.92^{+0.10}_{-0.11}$ | ⋯ |
| (2) | S1458-0023 | ⋯ | ⋯ | ⋯ | ⋯ | ⋯ |
| (2) | S1527+0652 | $8.53 \pm 0.10$ | PP04-N2 | ⋯ | ⋯ | ⋯ |
| (2) | S2111-0114 | ⋯ | ⋯ | ⋯ | ⋯ | ⋯ |
| (2) | Cosmic Eye | $8.02 \pm 0.30$ | KK04-R23-u | ⋯ | ⋯ | ⋯ |
| (2) | Planck Arc | $8.16 \pm 0.09$ | PP04-N2 | ⋯ | $7.52^{+0.04}_{-0.03}$ | ⋯ |
| (2) | PSZ0441 | ⋯ | ⋯ | ⋯ | ⋯ | ⋯ |
| (2) | SPT0310 | ⋯ | ⋯ | ⋯ | ⋯ | ⋯ |
| (2) | SPT2325 | ⋯ | ⋯ | ⋯ | ⋯ | ⋯ |
| (3) | A1689_876_330 | ⋯ | ⋯ | ⋯ | ⋯ | ⋯ |
| (3) | A1689_863_348 | ⋯ | ⋯ | $7.98^{+0.62}_{-0.09}$ | ⋯ | $8.58^{+0.26}_{-0.58}$ |
| (3) | A1689_860_359 | $\leqslant 8.54$ | KK04-R23-l | $8.19^{+0.75}_{-0.25}$ | ⋯ | $8.47^{+0.32}_{-0.34}$ |
| (3) | MACS0451_1.1 | $\leqslant 7.95$ | PP04-N2 | $8.06^{+0.52}_{-0.23}$ | $7.56^{+0.13}_{-0.11}$ | ⋯ |
| (4) | 2 | $7.81 \pm 0.07$ | direct | ⋯ | $7.91^{+0.03}_{-0.03}$ | $7.98^{+0.04}_{-0.03}$ |
| (4) | 36 | $7.92 \pm 0.04$ | direct | ⋯ | ⋯ | ⋯ |
| (4) | 80 | $8.24 \pm 0.06$ | direct | ⋯ | ⋯ | ⋯ |
| (4) | 82 | $7.91 \pm 0.04$ | direct | ⋯ | $8.12^{+0.02}_{-0.02}$ | $8.23^{+0.01}_{-0.01}$ |
| (4) | 110 | $8.17 \pm 0.08$ | direct | ⋯ | ⋯ | ⋯ |
| (4) | 111 | $7.81 \pm 0.08$ | direct | ⋯ | ⋯ | ⋯ |
| (4) | 179 | $8.35 \pm 0.07$ | direct | ⋯ | ⋯ | ⋯ |
| (4) | 182 | $8.01 \pm 0.04$ | direct | ⋯ | $7.94^{+0.00}_{-0.01}$ | $8.36^{+0.02}_{-0.02}$ |
| (4) | 191 | $8.30 \pm 0.07$ | direct | ⋯ | ⋯ | ⋯ |
| (4) | 198 | $8.48 \pm 0.11$ | direct | ⋯ | ⋯ | ⋯ |

**Table 3**
(Continued)

| References | Object | Optical Abundance | | UV 12 + $\log_{10}$(O/H) Abundance | | |
|---|---|---|---|---|---|---|
| | | 12 + $\log_{10}$(O/H) | Method | Si3–O3C3 | He2–O3C3 | C4–O3C3 |
| (5) | Q2343-BX418 | 7.90 ± 0.20 | direct | ⋯ | $7.54^{+0.07}_{-0.07}$ | ⋯ |
| (6) | A1689_31.1 | 7.69 ± 0.13 | direct | ⋯ | ⋯ | $8.69^{+0.52}_{-0.39}$ |
| (7) | SL2SJ0217 | ⩾7.50 | direct | $7.99^{+0.02}_{-0.03}$ | $7.60^{+0.01}_{-0.01}$ | $8.64^{+0.06}_{-0.04}$ |
| (8) | stack | 8.14 ± 0.04 | direct | $8.05^{+0.25}_{-0.13}$ | $8.16^{+0.22}_{-0.03}$ | ⋯ |
| (9) | SGASJ105039 | 8.26 ± 0.20 | KK04-R23-l | $8.24^{+0.59}_{-0.25}$ | $7.91^{+0.31}_{-0.14}$ | ⋯ |
| (10) | HS1442+4250 | 7.65 ± 0.04 | direct | ⋯ | $7.77^{+0.03}_{-0.03}$ | $8.19^{+0.00}_{-0.00}$ |
| (10) | J0405-3648 | 7.56 ± 0.07 | direct | ⋯ | ⋯ | ⋯ |
| (10) | J0940+2935 | 7.63 ± 0.14 | direct | ⋯ | ⋯ | ⋯ |
| (10) | J1119+5130 | 7.51 ± 0.07 | direct | ⋯ | ⋯ | ⋯ |
| (10) | SBSG1129+576 | 7.47 ± 0.06 | direct | ⋯ | ⋯ | ⋯ |
| (10) | UM133 | 7.70 ± 0.09 | direct | ⋯ | $7.89^{+0.05}_{-0.04}$ | ⋯ |

**References.** (1) Berg et al. (2016), (2) Rigby et al. (2018b), (3) Stark et al. (2014), (4) Senchyna et al. (2017), (5) Erb et al. (2010), (6) Christensen et al. (2012), (7) Berg et al. (2018), (8) Steidel et al. (2016), a stack of 30 galaxy spectra; (9) Bayliss et al. (2014), (10) Senchyna et al. (2019).

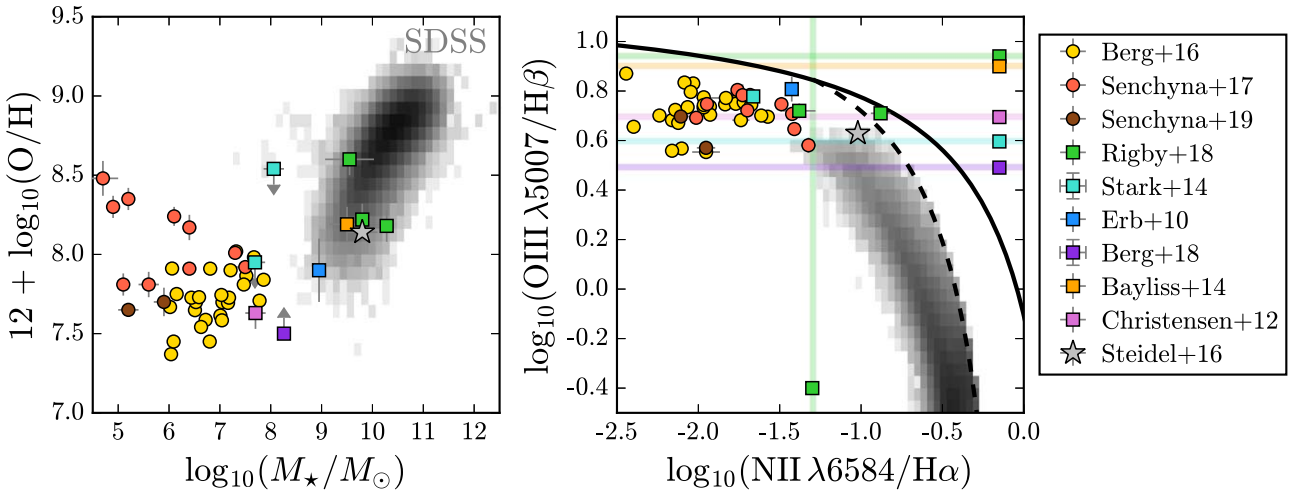


**Figure 1.** Left: stellar mass (*x*-axis) and optical gas-phase metallicity (*y*-axis) for the galaxies used in this work. The gray 2D histogram shows local star-forming galaxies from SDSS. For the galaxies considered in this work, the color of each marker indicates the source of the observation, compiled from the literature. Circular markers show local galaxies ($z < 0.1$) with rest-UV observations from HST/COS, while square markers show moderate-redshift galaxies with rest-UV spectra observed in the optical. For clarity, we only show those galaxies with robust UV and optical metallicities. The galaxies considered in this work have lower masses than typical star-forming galaxies in the local universe, but span a wide range in stellar mass and gas-phase metallicity. Overall, the low- and moderate-redshift galaxies occupy different regions of parameter space, with local galaxies having lower masses and metallicities. Right: the standard BPT diagram. The dashed line shows the Kauffmann et al. (2003) separation between the star formation and composite regions, and the solid black line shows the Kewley et al. (2001) separation between AGN and star formation. Horizontal lines are shown for objects without [N II]/H$\alpha$ measurements, and vertical lines are shown for objects without [O III]/H$\beta$ measurements. In general, the galaxies considered in this work have highly excited gas and lower metallicities than the typical star-forming galaxy in the local universe.

compared to 3 Å in Berg et al. 2016) allows the authors to simultaneously fit for broad and narrow emission-line components, when present. The published emission-line fluxes are not corrected for galactic or intrinsic extinction, but the authors provide their derived $E(B-V)$ for each object. We correct line fluxes for galactic and intrinsic extinction using the Fitzpatrick (1999) and Cardelli et al. (1989) reddening laws respectively, with $R_v = 3.1$. The optical emission-line ratios for the Senchyna et al. (2019) objects (used in Figure 1) were obtained via private communication.

### 3.2. Moderate-redshift Star-forming Galaxies

We use strongly lensed galaxies from Project MEGaSaURA: the Magellan Evolution of Galaxies Spectroscopic and Ultraviolet Reference Atlas (Rigby et al. 2018a, 2018b), spanning the redshift range $1.68 < z < 3.6$.

The MEGaSaURA galaxies have rest-UV spectroscopy taken with the MagE instrument on the Magellan telescopes. The spectra cover the wavelength range $3200 < \lambda < 8280$ Å in the observed frame (approximately $1000 \lesssim \lambda \lesssim 3000$ Å in the rest frame), with an average spectral resolving power of $R \sim 3300$ and S/N = 21 per resolution element in the median spectrum.

We include 4 of the 19 MEGaSaURA galaxies. Galaxies were excluded from the sample based on the following criteria:

1. Galaxies suspected to harbor low-luminosity active galactic nuclei (AGNs; $N = 2$).
2. Galaxies without rest-frame optical spectra ($N = 10$).

3. We require at least three UV emission lines to calculate the UV metallicity, and remove galaxies with fewer than three UV emission lines ($N = 3$).

The remaining four galaxies have rest-frame optical spectra from Keck NIRSPEC (Rigby et al. 2011; Wuyts et al. 2012), Keck OSIRIS (Wuyts et al. 2014), HST/WFC3 (Whitaker et al. 2014), LBT/LUCIFER (Bian et al. 2010), and Magellan FIRE spectrograph (Rivera-Thorsen et al. 2017).

UV emission-line fluxes for the MEGaSaURA galaxies are measured following Acharyya et al. (2019) and will be published in a future MEGaSaURA paper (J. Rigby et al. 2020, in preparation). The MEGaSaURA spectra have been corrected for foreground extinction using the galactic extinction from the Schlafly & Finkbeiner (2011) recalibration of the Schlegel et al. (1998) infrared-based dust map, assuming a Fitzpatrick (1999) reddening law with $R_v = 3.1$. Emission-line fluxes are dereddened using a Cardelli et al. (1989) dust curve using values of $E(B - V)$ derived from SED fitting (J. Rigby et al. 2020, in preparation).

*Other observations of moderate-redshift galaxies*—When possible, we also compare our models to the published emission-line fluxes for the four lensed galaxies from Stark et al. (2014) and the single lensed galaxies from Erb et al. (2010), Christensen et al. (2012), Bayliss et al. (2014), and Berg et al. (2018). We also include the stacked spectrum of lensed galaxies from Steidel et al. (2016); however, we note that it is much more difficult to interpret the metallicity derived from a stacked spectrum. Galaxies included in the sample are given in Table 3. For all objects, we use dereddened emission-line fluxes. In cases where dereddened line fluxes were not available in a published table, we dereddened emission-line fluxes following the original source's description.

Our requirement of three distinct UV emission-line detections limits the total number of objects in our sample, and we note that some of these references include additional objects with rest-UV and rest-optical spectra (e.g., Christensen et al. 2012) that we do not include in this work. A more complete list of objects with rest-UV and rest-optical spectra can be found in Patrício et al. (2019) and Plat et al. (2019).

### 3.3. Sample Global Properties and Caveats

In the left panel of Figure 1, we show the stellar mass and gas-phase metallicity for all of the galaxies included in our sample (see Table 3). The gray 2D histogram shows star-forming galaxies from SDSS (DR7; Abazajian et al. 2009). The color of each marker indicates the literature source for the observation and the shape of the marker separates nearby galaxies (circles) from moderate-redshift galaxies (squares). The UV–optical sample comprises galaxies with stellar masses between $10^{4.7}$ and $10^{10.3}\,M_\odot$ and gas-phase metallicities between $7.3 < 12 + \log_{10}(\mathrm{O/H}) < 8.6$.

The right panel of Figure 1 shows the standard Baldwin, Phillips, & Terlevich (BPT; Baldwin et al. 1981) diagram, which uses the [N II]/H$\alpha$ and [O III]/H$\beta$ emission-line ratios. We include empirically derived relationships used to separate objects with different ionizing sources; the dashed line shows the Kauffmann et al. (2003) separation between star formation and composite regions, and the solid black line shows the Kewley et al. (2001) separation between AGN and star formation. Some of the moderate-redshift galaxies are sufficiently distant such that the [N II] $\lambda$6584 and H$\alpha$ $\lambda$6563 emission lines have redshifted out of optical wavelengths and only have [O III] $\lambda$5007 and H$\beta$ $\lambda$4861 measurements. For these objects, we include a horizontal line at the measured [O III]/H$\beta$ ratio on the BPT diagram. For those objects without observations of [O III] $\lambda$5007 and H$\beta$ $\lambda$4861, we include a vertical line at the measured [N II]/H$\alpha$ ratio.

In general, the UV–optical sample has higher [O III]/H$\beta$ ratios and lower [N II]/H$\alpha$ ratios than the sample of local star-forming galaxies from SDSS. We note that both the Berg et al. (2016, 2019) and Senchyna et al. (2017, 2019) samples were designed to target high-ionization, high-excitation dwarf galaxies to maximize the detection of the UV C and O emission lines. Thus, their gas conditions are not representative of the local galaxy population as a whole. Optical emission-line diagnostic diagrams demonstrate that these objects have the expected properties of typical, metal-poor photoionized galaxies. We refer the reader to each of these publications for a comprehensive comparison of optical emission properties.

We utilize these samples for comparisons among UV and optical diagnostics only, and our conclusions cannot be inferred for samples outside the parameter ranges of these original samples. We also emphasize that the comparison of local and moderate-redshift samples in this work cannot be used to infer any meaningful cosmic evolution in ISM properties. There are a number of key differences between the local and moderate-redshift samples that may complicate our conclusions, which we state here.

First, the local BCDs have lower metallicities than the moderate-redshift galaxies. The local sample has oxygen abundances between $7.3 < 12 + \log_{10}(\mathrm{O/H}) < 8.2$ with a median of $12 + \log_{10}(\mathrm{O/H}) = 7.7$ and dispersion of 0.2 dex. The moderate-redshift sample has oxygen abundances between $7.6 < 12 + \log_{10}(\mathrm{O/H}) < 8.6$ with a median of $12 + \log_{10}(\mathrm{O/H}) = 8.2$ and a dispersion of 0.3 dex.

The second major difference between low- and moderate-redshift galaxies is the typical stellar mass. The low-redshift galaxies are all of very low mass, $M \lesssim 10^{7.5}\,M_\odot$.[10] In contrast, the moderate-redshift galaxies have higher stellar masses, $M \gtrsim 10^{7.5}\,M_\odot$. Thus, we are not comparing the same types of galaxies in this analysis, and any perceived correlations with redshift will not actually reveal any information about the evolution of the ISM. In general, however, the galaxies considered in this work have lower masses than typical star-forming galaxies from the SDSS survey. Both the low- and moderate-redshift samples have masses more typical of local dwarf galaxies (e.g., Lee et al. 2006; Berg et al. 2012).

We note that there are a few objects with $M \lesssim 10^{5.5}\,M_\odot$ from Senchyna et al. (2017; e.g., SB 179, 191, 198). These objects are giant H II regions embedded within larger disk systems, with physical scales of order 100 pc.

## 4. Metallicity Determinations

### 4.1. Theoretical Metallicity Calibrations

There is a known offset among theoretical abundances (i.e., the true specified gas-phase abundances in photoionization models) and the abundances calculated from strong-line and direct-temperature methods (i.e., the gas-phase abundances one would compute from the models based on emission-line

[10] We note that the mass estimates from SDSS for the lowest-mass systems ($M \lesssim 10^7\,M_\odot$) are likely underestimated, due to the reduced accuracy in redshift as a distance indicator (e.g., Mamon et al. 2019).

strengths), as discussed in Stasińska (2005) and Kewley & Ellison (2008; and references therein). It has been suggested that this offset is the result of temperature gradients within the nebulae that bias the characteristic temperature of a given line transition away from the mean ionic temperature (e.g., Stasińska 2005; Bresolin 2007; Kewley & Ellison 2008); though it has also been attributed to an unknown issue with photoionization models (e.g., Kennicutt et al. 2003).

In practice, we put our model metallicities onto the same scale as the observed metallicities by applying the same analysis techniques used on observations, which we describe below. In general, the correction to model metallicities is small, $\lesssim$0.1 dex for $\log_{10}(\mathrm{O/H}) \lesssim 8$. The correction is larger at metallicities $\log_{10}(\mathrm{O/H}) \gtrsim 8.7$, between 0.2 and 1.0 dex, depending on the model ionization parameter, where models with higher ionization parameters require larger corrections. We describe the correction calculation for direct-$T_e$ and strong-line abundances below.

#### 4.1.1. Direct-$T_e$ Theoretical Calibration

At each age, metallicity, and ionization parameter point in the **CloudyFSPS** model grid, we calculate an optical direct-method abundance to determine the offset between the true oxygen abundance in the CLOUDY model and the measured oxygen abundance. Using least-squares minimization (`numpy.polyfit`), we fit a third-order polynomial to the direct-temperature oxygen abundance as a function of the true CLOUDY oxygen abundance at each model age and ionization parameter. We provide the polynomial fits in Appendix A.

For the closest comparison between the models and the observational samples, we calculate direct-$T_e$ abundances for our models following the method used in Garnett (1992), as modified by Berg et al. (2015) and applied to the Berg et al. (2016, 2019) observations. We briefly describe the process below.

We calculate gas-phase oxygen abundances using a two-temperature-zone approximation with `PyNeb` (Luridiana et al. 2013) and collision strengths from Aggarwal & Keenan (1999). We use the Aggarwal & Keenan (1999) collision strengths rather than the newer Storey et al. (2014) collision strengths, as the Aggarwal & Keenan (1999) collision strengths are calculated for a six-level oxygen atom, which is needed for the UV [O III] $\lambda$1661,1666 lines ($^5S_2 \rightarrow {}^3P_2$ and $^5S_2 \rightarrow {}^3P_1$ transitions, respectively).

Following Garnett (1992) and Berg et al. (2015), we approximate the H II region with a high- and low-temperature zone for the $O^{++}$ and $O^+$ regions, respectively.

For the $O^+$ zone, we calculate the density using the [S II] $\lambda$6731/[S II] $\lambda$6716 ratio. For the $O^+$ zone temperature, we use ([N II] $\lambda$6548 + [N II] $\lambda$6584)/[N II] $\lambda$5755 following the recommendation of Berg et al. (2015). The $O^+$ ionic abundance is then calculated with `PyNeb`, using the line intensities

$$\left[\frac{\mathrm{O}^+}{\mathrm{H}^+}\right] = \frac{I_{\lambda\lambda\ 3727,3729} + I_{\lambda\lambda\ 7319,7332}}{I_{\mathrm{H}\beta}} \cdot \frac{j_{\mathrm{H}\beta}}{j_\lambda}. \quad (3)$$

For the $O^{++}$ zone, we calculate the density using the [S II] $\lambda$6731/[S II] $\lambda$6716 ratio. For the $O^{++}$ zone temperature, we use the [O III]$\lambda$4363/([O III]$\lambda$4959 + [O III]$\lambda$5007) ratio. The $O^{++}$ ionic abundance is then calculated with `PyNeb`, using the line intensities

$$\left[\frac{\mathrm{O}^{++}}{\mathrm{H}^+}\right] = \frac{I_{\lambda\ 4363} + I_{\lambda\ 4959} + I_{\lambda\ 5007}}{I_{\mathrm{H}\beta}} \cdot \frac{j_{\mathrm{H}\beta}}{j_\lambda}. \quad (4)$$

The total oxygen abundance is then calculated as the sum of the ionic abundances,

$$\log_{10}(\mathrm{O/H}) = \left[\frac{\mathrm{O}^{++}}{\mathrm{H}^+}\right] + \left[\frac{\mathrm{O}^+}{\mathrm{H}^+}\right], \quad (5)$$

assuming a negligible contribution from $O^0$ and $O^{+++}$ ions, appropriate for most H II regions (Berg et al. 2016). We note that the model calibrations do not change if we include the contribution from $O^{+++}$ ions. In the models used here, $O^{+++}/H^+$ is of order $10^{-8}$ and is never larger than $10^{-7}$.

In Appendix B, we provide a comparison of theoretical direct-$T_e$ abundances using UV and optical emission lines.

#### 4.1.2. Strong-line Theoretical Calibration

Some of the galaxies in the moderate-redshift sample have metallicities calculated from optical strong-line methods. To avoid introducing additional uncertainties into the comparison from using abundances that have been empirically corrected to a "standard" abundance scale, we recompute the optical abundances using the published optical emission-line strengths and the Pettini & Pagel (2004, hereafter PP04) N2 abundance scale.

We have chosen the PP04-N2 abundance scale because it maximizes the number of objects in the moderate-redshift sample that have optical metallicities that can be computed using the same method. As noted in Section 3.3, several galaxies in the moderate-redshift sample do not have [N II]/H$\alpha$ measurements. However, even fewer galaxies have observations of the [O II]$\lambda$3726,3729 doublet required for $R_{23}$ metallicities.

It is not clear which, if any, of the metallicity scales is correct. As such, only relative metallicities (i.e., metallicities calculated using the same method) provide a reliable comparison. We note that the PP04-N2 abundance scale does not account for ionization parameter changes, which is particularly important for low-metallicity galaxies and galaxies at high redshift where the ionization parameter is typically high (e.g., Kewley et al. 2013a, 2013b; Masters et al. 2014; Sanders et al. 2016; Bian et al. 2017; Strom et al. 2017), and likely larger than those in the H II regions used by PP04 to make their N2 calibration.

At each metallicity and ionization parameter point in the **CloudyFSPS** model grid, we use the model emission-line fluxes to calculate a PP04-N2 abundance using the equation from PP04:

$$12 + \log_{10}(\mathrm{O/H}) = 0.57 \cdot \log_{10}([\mathrm{N\ II}]\lambda6584/\mathrm{H}\alpha) + 8.90. \quad (6)$$

To determine the offset between the PP04-N2 oxygen abundance and the true CLOUDY oxygen abundance, we fit a linear function to the PP04-N2 abundance as a function of the CLOUDY oxygen abundance for each of the ionization parameters in the model. The best-fit parameters for the linear function are determined using least-squares minimization with (`numpy.polyfit`).

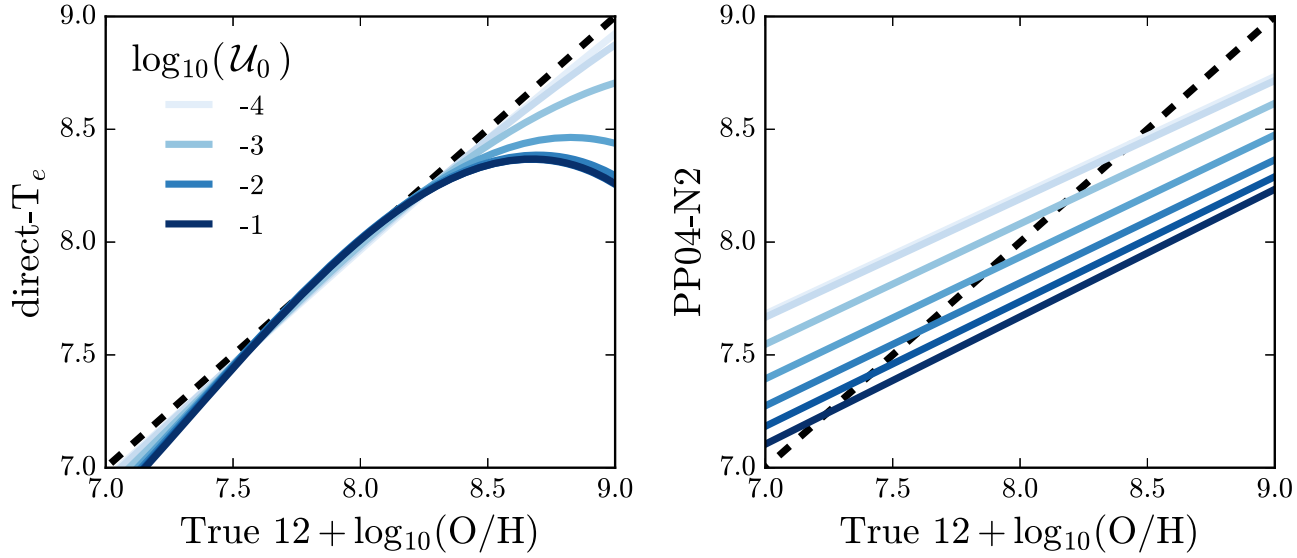


**Figure 2.** Metallicity offsets for the direct-$T_e$ method (left) and the PP04-N2 method (right). The $x$-axis shows the true gas-phase oxygen abundance from CLOUDY. The $y$-axis shows the metallicity derived from emission-line strengths using the respective metallicity calculations. Each line represents the polynomial fit to the models at different ionization parameters, for a model with constant SFR over 10 Myr. The lines are color-coded by ionization parameter, from $\log_{10}\mathcal{U}_0 = -4$ in light blue to $\log_{10}\mathcal{U}_0 = -1$ in dark blue. The black dashed line shows a one-to-one relationship.

We show the resultant PP04-N2 calibration for the 10 Myr constant-SFR models used in this work in Figure 2, following Figure 1 of Stasińska (2005). The $x$-axis shows the "true" oxygen abundance, as input to CLOUDY, and the $y$-axis shows the abundance calculated from the direct-$T_e$ method (left) and the PP04-N2 method (right). In both panels, the blue lines show the fit used for the theoretical correction, color-coded by ionization parameter. The fitted line is a third-order polynomial for direct-$T_e$ abundances (left) and a linear function for the strong-line abundances (right). These fits are provided in Appendix A, Tables A1 and A2.

The Cosmic Eye galaxy, SGASJ105039, and A1689_860_359 are the only objects with 3+ UV emission lines where we could not calculate a PP04-N2 abundance, because the necessary [N II] and H$\alpha$ lines have been redshifted out of the optical observing window.[11] Instead, we repeat the above process using the Kobulnicky & Kewley (2004) R23 abundance scale (hereafter KK04-R23), assuming the upper branch for Cosmic Eye and SGASJ105039, and the lower branch for A1689_860_359. The fits for the KK04-R23 are provided in Appendix A, Table A3. For each object in the sample, Table 3 includes the method used for the optical abundance determination.

### 4.2. Deriving Abundances from UV Diagnostic Diagrams

In this section, we derive gas-phase abundances for the galaxies in the sample using rest-frame UV emission lines. We use different combinations of predicted emission-line ratios to construct "diagnostic diagrams." At a given model age, variations in ionization parameter and metallicity change the predicted emission-line ratios, producing a grid or surface in the diagnostic diagram. Then, for each galaxy, we compare the observed emission-line ratios to the model emission-line ratios to calculate a gas-phase abundance. Specifically, the emission-line ratios ($x$, $y$) for a given galaxy are matched to the surface of the model grid by interpolating between points in ionization parameter and metallicity using the `scipy.interpolate.griddata` cubic spline interpolation.

This approach can be sensitive to small changes in the observed emission-line ratios, so we use a Monte Carlo method to estimate errors on the derived metallicity. For each object, we draw $N = 1000$ samples from a Gaussian distribution centered at the observed line ratio ($x$, $y$) and width equal to the reported emission-line ratio errors. We then recalculate the metallicity at each of these 1000 samples and use the spread in the resultant metallicity distribution to estimate errors, where the 16th and 84th percentiles of the metallicity distribution provide the upper and lower error limits, respectively.

We then rescale the metallicity using the theoretical abundance calibrations derived in Section 4.1, so that we can compare the UV-derived abundance to the abundances derived using optical emission lines. For the nearby galaxies with optical direct-$T_e$ metallicities, we apply the direct-$T_e$ correction described in Section 4.1.1. For the moderate-redshift galaxies with optical strong-line metallicities, we apply the relevant strong-line correction described in Section 4.1.2. In general, the metallicity correction changes the UV-derived abundance by $<$0.1 dex at $12 + \log_{10}(\mathrm{O/H}) < 8$, and by $\sim$0.1 dex at $8.0 < 12 + \log_{10}(\mathrm{O/H}) < 8.5$.

The calculated gas-phase oxygen abundances for the observational comparison sample are given in Table 3.

## 5. UV–Optical Abundance Comparisons

In this section, we compare the metallicities derived with UV emission lines (Section 4.2) to those derived with optical emission lines, to evaluate the utility of UV diagnostic diagrams as metallicity indicators.

Our UV–optical sample requires three significant emission-line detections in the UV. Across the sample, C III] $\lambda$1906,1909 and [O III] $\lambda$1666 were the most commonly detected emission lines. This is not surprising, given that the C III] $\lambda$1906,1909 doublet is the brightest emission line in the UV spectra of star-forming galaxies after Ly$\alpha$. As such, a number of authors have

[11] This is also true for the MEGaSaURA galaxy S1226+2152; however this object does not have enough UV emission-line detections to derive a UV metallicity and could not be included in the UV–optical comparison.

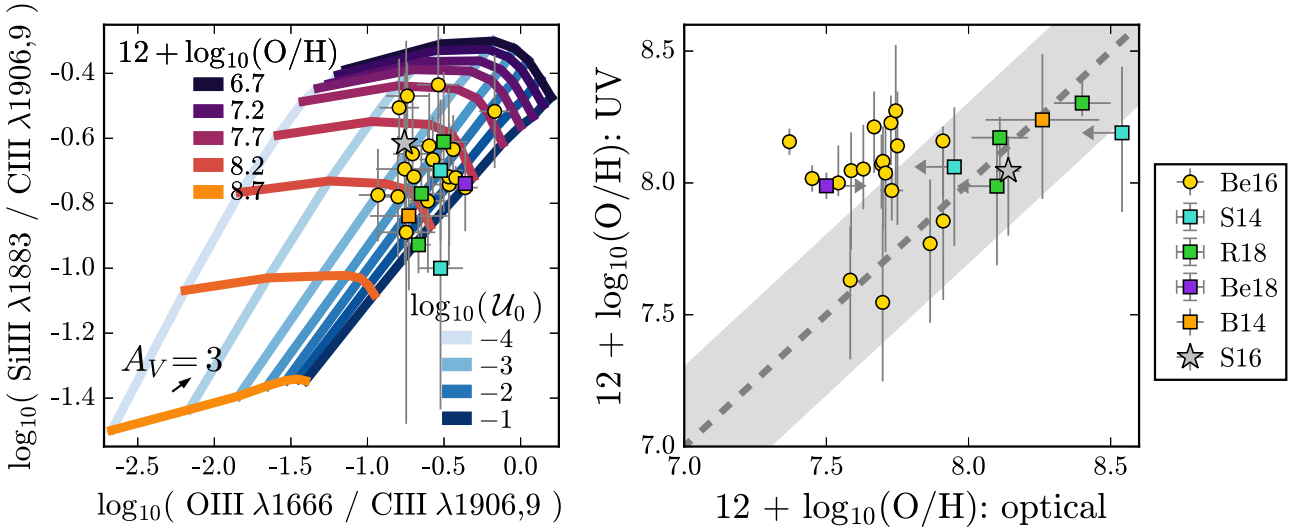


**Figure 3.** Left: Si3–O3C3 UV diagnostic diagram, as presented in B18. The blue lines connect models of constant ionization parameter, from $\log_{10}\mathcal{U}_0 = -1$ (dark blue) to $\log_{10}\mathcal{U}_0 = -4$ (light blue). Models of constant metallicity are shown from $12 + \log_{10}(\mathrm{O/H}) = 6.69$ ($\log_{10} Z/Z_\odot = -2$; purple) to $12 + \log_{10}(\mathrm{O/H}) = 8.69$ ($\log_{10} Z/Z_\odot = 0$; orange). Right: metallicity derived using the Si3–O3C3 UV diagnostic (*y*-axis) compared to the optically derived metallicity (*x*-axis). The dashed line shows a one-to-one relationship, and a 0.3 dex spread is shown by the gray shaded region. Identical symbols are used for the galaxy sample in both panels. Low-redshift galaxies from Berg et al. (2016, 2019) are shown with gold circles. Moderate-redshift galaxies are shown with squares, from Stark et al. (2014, cyan), Bayliss et al. (2014, orange), Rigby et al. (2018a, green), and Berg et al. (2018, purple). The gray star is the stacked spectrum of moderate-redshift galaxies from Steidel et al. (2016).

suggested emission-line diagnostics that make use of the C III] λ1906,1909 doublet (e.g., Feltre et al. 2016; Jaskot & Ravindranath 2016; Byler et al. 2018; Hirschmann et al. 2019).

In Sections 5.1–5.3, we highlight three UV diagnostic diagrams that use the C III] λ1906,1909 and [O III] λ1666 lines paired with a third emission line: [Si III] λ1893 (Section 5.1), He II λ1640 (Section 5.2), and the C IV λ1548,1550 doublet (Section 5.3).

### 5.1. [Si III] λ1883,1893

In B18, we highlighted the potential of the [Si III] λ1883/C III] λ1906 (Si3C3) versus [O III] λ1666/C III] λ1906 (O3C3) diagnostic diagram. These emission lines are relatively bright and easy to detect, and are closely spaced in wavelength to minimize dust extinction errors.

In the left panel of Figure 3, we show the Si3–O3C3 diagnostic diagram as presented in B18. We compare the model grid with the observed galaxy sample, where the nearby galaxies are shown with circular markers and moderate-redshift galaxies are shown with square markers, including Berg et al. (2016, B16, 2019; gold circles), Rigby et al. (2018a, R18; green squares), Stark et al. (2014, S14; cyan squares), and Berg et al. (2018, Be18; purple square). The stacked spectrum from Steidel et al. (2016, S16) is shown by the gray star. As noted in B18, the model grid is able to reproduce the observed range of line ratios in samples of both low- and moderate-redshift galaxies.

The right panel of Figure 3 shows the comparison between optical metallicity (*x*-axis) and UV metallicity (*y*-axis) derived with the Si3–O3C3 diagnostic. Galaxy observations are shown with the same marker shapes and colors as in the left panel, and the black dashed line shows a one-to-one correlation between UV and optical metallicities. The gray shaded region shows a 0.3 dex spread from the one-to-one relationship. In some cases, the optical metallicity errors may be underestimated, and ±0.3 dex represents the typical systematic errors inherent in optical strong-line methods (Kewley et al. 2019b).

The UV and optical metallicities agree within error for 13 of the 26 galaxies (50%). In general, the UV metallicity is biased toward higher values, with a median offset of 0.35 dex from optical metallicities. The UV metallicities show significant scatter and are only marginally positively correlated with optical measurements, with a Spearman correlation coefficient of 0.26. Additionally, there are several objects (S14, Be18) where the UV metallicity catastrophically fails to match the optical metallicity. However, these failures do not seem to have an overall bias toward higher or lower metallicities.

In general, we do not necessarily expect the UV and optical abundances to exactly match, because many bright UV emission lines (e.g., C III]) are relatively high-ionization species. These high-ionization lines may reflect conditions in the inner part of the nebula where the gas is more highly ionized than in the regions probed by optical lines, leading to an offset between UV and optical metallicity. In the case of the direct-$T_e$ method, the metallicity offset is driven by temperature differences; for strong-line methods, the offset would be driven by variations in ionization parameter that are not accounted for in the optical metallicity diagnostic. However, most of the galaxies in this sample are relatively high-excitation objects, with temperatures dominated by the high-excitation zone. Moreover, the scatter in UV-derived abundances for a comparatively narrow range in optical abundance is surprising and suggests that the source of metallicity discrepancy has a different origin. It is possible that the scatter in Si3–O3C3 metallicities is the result of variation in elemental abundances ( i.e., carbon or silicon relative to oxygen) or in the dust depletion factors, as both carbon and silicon are expected to be heavily depleted from the gas phase onto dust grains.

We discuss the Si3–O3C3 metallicities in more detail in Section 6, where we use rest-optical spectroscopy from the Berg et al. (2016, 2019) sample to better understand the source of the scatter.

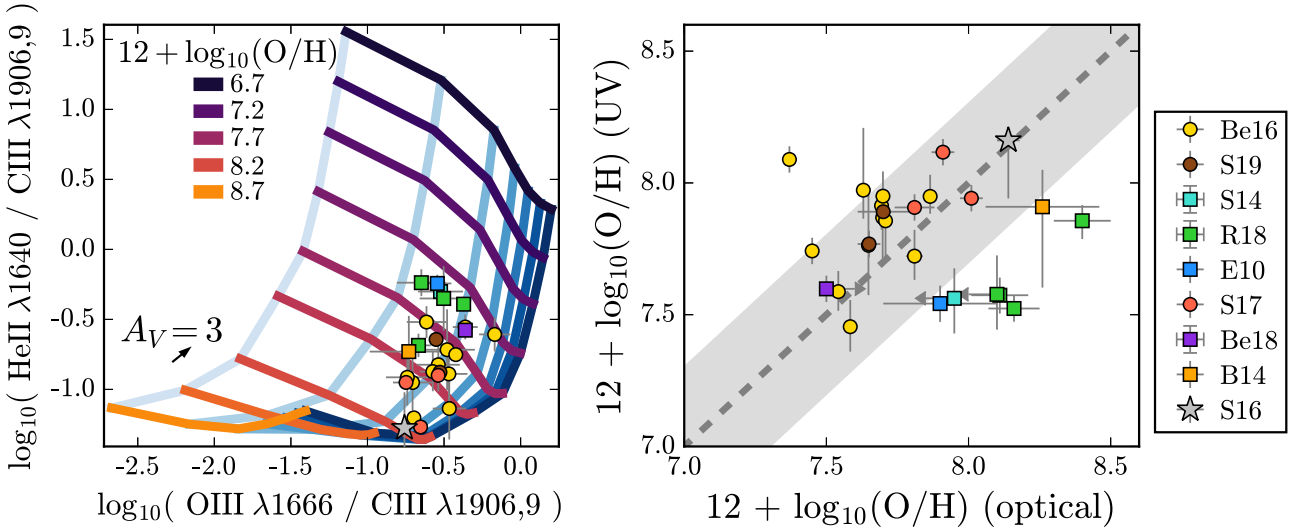


**Figure 4.** Left: the He2–O3C3 diagnostic diagram, with the model grid as described in the caption of Figure 3. Right: metallicity derived with the He2–O3C3 diagnostic (*y*-axis) compared to the optical metallicity (*x*-axis), where the dashed line shows a one-to-one relationship. The UV and optical metallicities are well matched for most of the galaxies, particularly the metal-poor objects. For the comparatively metal-rich MEGaSaURA galaxies (green squares), the UV diagnostic significantly underpredicts optical metallicities.

### 5.2. He II λ1640

He II λ1640 emission has been detected locally and at high redshift, and is one of the brighter UV emission lines. The He II λ1640 line has been used in several proposed emission-line diagnostics (e.g., Feltre et al. 2016; Jaskot & Ravindranath 2016), including the He2–O3C3 diagnostic presented in B18, which uses the He II λ1640, C III] λ1906,9, and [O III] λ1666 emission lines. In B18, however, we noted that observations of He II λ1640 emission can include contributions from both nebular emission and stellar wind emission, making it a potentially problematic metallicity tracer.

We assess the He2–O3C3 diagnostic in Figure 4, following the format of Figure 3, where the left panel shows the diagnostic diagram and the right panel shows the comparison between UV and optical metallicity.

In general, the agreement between the UV and optical metallicities with the He2–O3C3 diagnostic is improved over the Si3–O3C3 diagnostic. The UV metallicities in the right panel of Figure 4 show a stronger correlation with the optical metallicity (with a Spearman correlation coefficient of 0.3) and have a median offset of 0.1 dex. However, there are still three objects where the UV metallicity is entirely at odds with the optical abundance. Specifically, for the E10, B14, and R18 galaxies (blue, orange, and green squares, respectively), the UV abundance is systematically lower than the optical abundance by 0.3–0.6 dex.

The source of He II emission is a subject of ongoing debate, and He II emission is difficult to produce with current models, both stellar and nebular. Narrow He II emission is generally interpreted as having a nebular origin and requires significant numbers of high-energy photons. With currently available stellar models, very hard ionizing spectra require the presence of stellar multiplicity, stellar rotation, or very massive stars (e.g., Stark et al. 2014; Steidel et al. 2016; Byler et al. 2017; Choi et al. 2017).

Broad He II emission in galaxies is commonly interpreted as an indication of the presence of W-R stars (e.g., Kunth & Joubert 1985; Conti 1991; Schaerer et al. 1999; Brinchmann et al. 2008). W-R stars are more common in metal-rich stellar populations ($12 + \log_{10}(\mathrm{O/H}) \gtrsim 8$), with the strongest He II emission associated with populations at solar metallicity or higher.

With the exception of the Senchyna et al. (2017) and Berg et al. (2018) spectra (red circles and purple square, respectively), none of the spectra in the sample has fit separate components for broad and narrow He II emission. Most of the Berg et al. (2016, 2019) galaxies (gold circles) have low-enough metallicities that the "contamination" from stellar emission should be small (∼25% or less of the nebular emission flux), and there is no evidence that the He II emission is any broader than the other nebular emission lines. If broad He II were responsible for artificially inflating the observed He II λ1640 fluxes, we might expect that the contamination would be worse for the relatively metal-rich MEGaSaURA galaxies (R18, green squares).

We note that the stacked spectrum from Steidel et al. (2016) has a relatively high metallicity but does not seem to suffer from underpredicted UV metallicities like the MEGaSaURA galaxies. However, as a composite spectrum, it is difficult to extrapolate how light-weighted changes from the stellar continuum and nebular components ultimately impact the relative line strengths.

We discuss the nature of the He II emission at length in Section 6.3, where we compare the predictions from rotating stellar populations (used in this section) to predictions from binary stellar models, which have harder ionizing spectra at older ages. We also assess the level of contamination from broad stellar emission using a "wind-contaminated" emission-line grid.

The He2–O3C3 diagram shows promise as an oxygen abundance diagnostic, especially at low metallicities, where the stellar contribution is minimal ($12 + \log_{10}(\mathrm{O/H}) \lesssim 8$). However, a more detailed understanding of the various mechanisms responsible for He II photon production is required before the He3-O3C3 diagnostic can be applied to large samples with confidence.

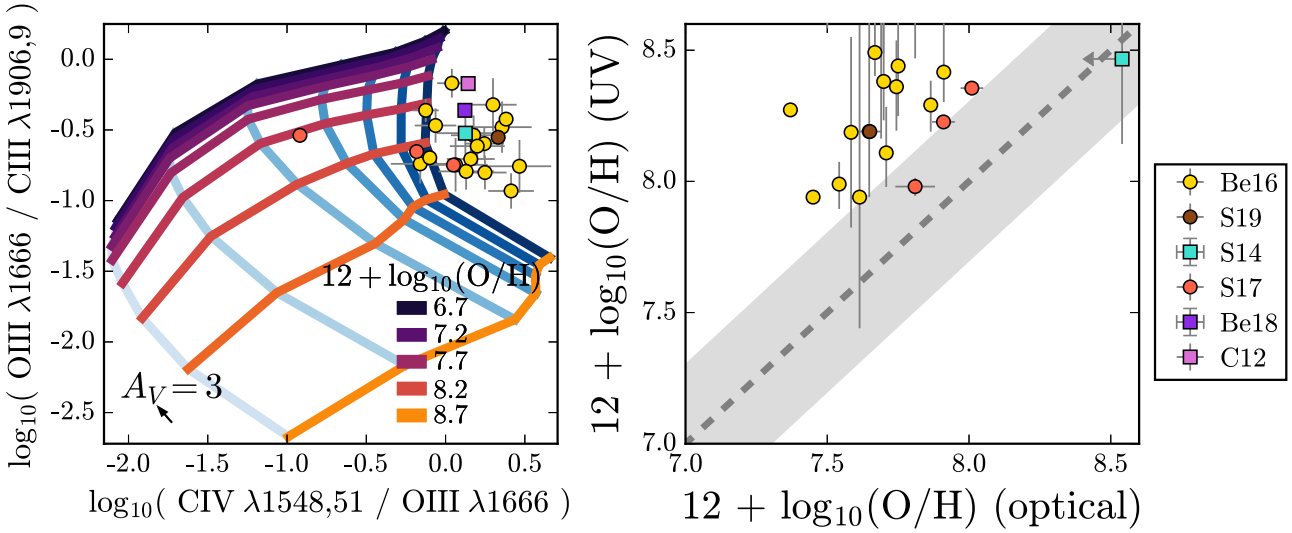


**Figure 5.** Left: the C4–O3C3 diagnostic diagram, with the model grid as described in the caption of Figure 3. Many of the galaxies have larger-than-predicted C4O3 ratios, in some cases due to contamination from stellar wind emission to the C IV emission line, though harder ionizing spectra could also help explain the offset. Right: metallicities predicted by the C4–O3C3 diagnostic compared to optically derived metallicities. The dashed line shows a one-to-one relationship. The UV diagnostic predicts metallicities that are poorly correlated with optical metallicities and offset by 0.3–0.5 dex.

### 5.3. C IV λ1548,1550

In this section, we assess the utility of the C4–O3C3 diagnostic, which uses the C IV $\lambda$ 1548,1550/[O III] $\lambda$ 1666 and [O III] $\lambda$ 1666/C III] $\lambda$ 1906,1909 emission-line ratios. The left panel of Figure 5 shows the model grid and observed emission-line ratios. Unlike Figures 3 and 4, the model grid is unable to reproduce the range of observed emission-line ratios, as noted in B18. Here, 70% of the galaxies have larger C4O3 ratios than predicted by the models.

The right panel of Figure 5 shows the comparison between UV and optical metallicities for the C4–O3C3 diagnostic. Unsurprisingly, the mismatch between observed and model line ratios translates to poor agreement between the UV and optical metallicities in the right panel. For nearly all objects, the UV metallicity is larger than the optical metallicity, by 0.1–0.7 dex, with an average offset of 0.5 dex. Only two objects have UV metallicities consistent with their optical estimates within errors. Additionally, there is some evidence for a metallicity-dependent offset, where the metal-rich objects show somewhat more scatter.

C IV emission is one of the more difficult spectral features to interpret, due to the competing effects of nebular emission at 1548 and 1550 Å, stellar wind emission at 1550 Å (often broad, with a strong P-Cygni profile), and interstellar absorption between 1545 and 1550 Å. Generally, the strength of the nebular C IV emission peaks at low metallicity ($12 + \log_{10}(\mathrm{O/H}) \sim 7$) and high ionization parameter ($\log_{10}\mathcal{U}_0 \gtrsim -2$). In contrast, stellar emission is wind driven and strongest at higher metallicities, solar like and above. However, even at $12 + \log_{10}(\mathrm{O/H}) = 7.5$ ($\log_{10} Z/Z_\odot \sim -1$), stellar C IV emission can account for as much as 30% of the total C IV emission (B18). Interstellar absorption plays an important role at higher metallicities (solar like and above), where it can dominate the composite C IV spectral feature. ISM absorption must be accounted for when making integrated line index measurements (e.g., Vidal-García et al. 2017); however, $R > 1000$ is generally sufficient to distinguish the narrow interstellar absorption from the broad P-Cygni absorption (e.g., Crowther et al. 2006; Chisholm et al. 2019).

At the metallicities associated with the nearby galaxy sample ($12 + \log_{10}(\mathrm{O/H}) \sim 7.5$–8; yellow and red circles), the `MIST +wind` C IV emission models from B18 predict that stellar contamination can change the C4O3 ratio by 0.1–0.3 dex. We note that contamination from stellar emission should be less of an issue for the Senchyna et al. (2017) galaxies (red circles), because these observations fit for both broad and narrow C IV components. The C IV flux used in the line ratios from Figure 5 is that of the narrow, nebular C IV only. Encouragingly, the Senchyna et al. (2017) galaxies do show the smallest offset, potentially due to the fact that the C IV emission-line fluxes are a better representation of the uncontaminated nebular flux.

We note the absence of the MEGaSaURA galaxies in Figure 5. Inspection of the C IV emission feature in these comparatively metal-rich objects reveals strong stellar emission with the signature P-Cygni profile, and little or no evidence for nebular emission[12] (Chisholm et al. 2019).

In Section 6, we test whether harder ionizing spectra or stellar wind contamination can ameliorate the mismatch between model and data C IV line strengths.

### 5.4. Abundance Determination Equations

As described in Section 4, the UV oxygen abundances presented in Table 3 are calculated by interpolating the model grid. For users who wish to replicate this process on their own data, the model emission-line ratios were published in B18 and are publicly available.

To facilitate abundance determinations for the UV diagnostics discussed in this work, we also provide a simple functional form for the diagnostic diagrams shown in Figures 3 and 4. Using `Polynomial2D` from `astropy.models`, we fit a third-degree 2D polynomial to the model grid surface with a Levenberg–Marquardt algorithm and least-squares statistic from `astropy.fitting`. These fits are valid for objects with $6.2 \leqslant 12 + \log_{10}(\mathrm{O/H}) \leqslant 9.2$, and $-4.0 \leqslant \log_{10}\mathcal{U}_0 \leqslant -1.0$. These fits should only be applied to objects with observed line

[12] With the exception of RCS0327-G, which does not have a matched optical metallicity.

**Table 4**
Coefficients for the Third-degree 2D Polynomial Fit to the Model Grid Surfaces

| | Si3–O3C3 | He2–O3C3 |
|---|---|---|
| c0_0 | 3.09 | 6.88 |
| c1_0 | 0.09 | −1.13 |
| c2_0 | −1.71 | −0.46 |
| c3_0 | −0.73 | −0.03 |
| c0_1 | −16.51 | −0.61 |
| c0_2 | −19.84 | 0.02 |
| c0_3 | −6.26 | −0.04 |
| c1_1 | 4.79 | −0.32 |
| c1_2 | −0.28 | 0.03 |
| c2_1 | 1.67 | −0.21 |

ratios that are well described by the model grid (i.e., extrapolation to off-grid data points is not valid).

For the Si3–O3C3 diagnostic (Section 5.1), the fit yields

$$12 + \log_{10}(\mathrm{O/H}) = 3.09 + 0.09x - 1.71x^2 - 0.73x^3 - 16.51y - 19.84y^2 - 6.26y^3\ 4.79xy - 0.28xy^2 + 1.67x^2y, \quad (7)$$

where $x$ is $\log_{10}([\mathrm{O\ III}]\ \lambda1666/\mathrm{C\ III}]\ \lambda1906{,}9)$ and $y$ is $\log_{10}([\mathrm{Si\ III}]\ \lambda1883/\mathrm{C\ III}]\ \lambda1906{,}9)$. Typical statistical errors are $\pm0.14$ dex.

For the He2–O3C3 diagnostic (Section 5.2), the fit yields

$$12 + \log_{10}(\mathrm{O/H}) = 6.88 + -1.13x - 0.46x^2 - 0.03x^3 - 0.61y + 0.02y^2 - 0.04y^3 - 0.32xy + 0.03xy^2 - 0.21x^2y, \quad (8)$$

where $x$ is $\log_{10}([\mathrm{O\ III}]\ \lambda1666/\mathrm{C\ III}]\ \lambda1906{,}9)$ and $y$ is $\log_{10}(\mathrm{He\ II}\ \lambda1640/\mathrm{C\ III}]\ \lambda1906{,}9)$. Typical statistical errors are $\pm0.08$ dex.

We do not provide an equation for the C4–O3C3 diagnostic (Section 5.3), because the model grid does not satisfactorily cover the observed parameter space, which we discuss in Section 6.4.

We note that the oxygen abundances obtained with Equations (7) and (8) will not be identical to those obtained from the direct interpolation of the model grid. However, the oxygen abundances from the two methods are tightly correlated, with 0.11 and 0.03 dex scatter for Si3–O3C3 (Equation (7)) and He2–O3C3 (Equation (8)), respectively. For the Si3–O3C3 diagnostic, this scatter can be reduced to 0.06 dex by using a fourth-degree 2D polynomial, which increases the number of terms in the equation from 10 to a more unwieldy 15. We provide the coefficients for all fits in Tables 4 and 5, following the form for a general polynomial of degree $n$[13]:

$$P(x, y) = c_{00} + c_{10}x + ... + c_{n0}x^n + c_{01}y + ... + c_{0n}y^n + c_{11}xy + c_{12}xy^2 + ... + c_{1(n-1)}xy^{n-1} + ... + c_{(n-1)1}x^{n-1}y. \quad (9)$$

**Table 5**
Coefficients for the Fourth-degree 2D Polynomial Fit to the Model Grid Surfaces

| | Si3–O3C3 | He2–O3C3 |
|---|---|---|
| c0_0 | −0.29 | 6.88 |
| c1_0 | 1.23 | −1.28 |
| c2_0 | −5.11 | −0.74 |
| c3_0 | −2.58 | −0.14 |
| c4_0 | 1.01 | 0.01 |
| c0_1 | −40.48 | −0.59 |
| c0_2 | −80.57 | 0.06 |
| c0_3 | −65.69 | −0.04 |
| c0_4 | −13.78 | 0.03 |
| c1_1 | 17.89 | −0.30 |
| c1_2 | 15.28 | 0.33 |
| c1_3 | −11.48 | 0.00 |
| c2_1 | 1.67 | −0.44 |
| c2_2 | 18.33 | 0.20 |
| c3_1 | −8.27 | −0.18 |

A comparison of the oxygen abundances derived with Equations (7) and (8) is shown in Figure 6. The abundance derived from the direct interpolation of the model grid is shown on the $x$-axis and the oxygen abundance derived from the polynomial fit is shown on the $y$-axis. The Si3–O3C3 diagnostic is shown in the left column, and the He2–O3C3 diagnostic is shown in the right column. For each diagnostic, the third-degree 2D polynomial is shown on the top (Table 4) and the fourth-degree 2D polynomial is shown on the bottom (Table 5).

## 6. Discussion

### 6.1. The Silicon Discrepancy

The galaxies in the Berg sample have a fairly narrow range in optically derived nebular properties, with high ionization parameters ($-2.8 \lesssim \log_{10}\mathcal{U}_0 \lesssim -1.8$) and low metallicities ($7.5 \lesssim 12 + \log_{10}(\mathrm{O/H}) \lesssim 8$). We would thus expect UV-derived metallicities for these objects to reflect the similarity in gas properties. However, the metallicities derived using the [Si III]$\lambda$1883 line show a 0.2 dex larger scatter and appear to have a bimodal distribution (Figure 3).

The spread in UV-derived metallicities could be explained by variations in gas-phase silicon abundance relative to oxygen within the Berg sample. Silicon is an $\alpha$ element, and such variations could be the result of chemical evolution driven by star formation. However, silicon is also one of the main components of cosmic dust, which complicates abundance determinations.

[13] Quick-start for Python users: Create a dictionary of coefficient names and values from either Tables 4 or 5, "`coeffs`." Input this dictionary to `Polynomial2D(degree, **coeffs)` from `astropy.modeling.models`.

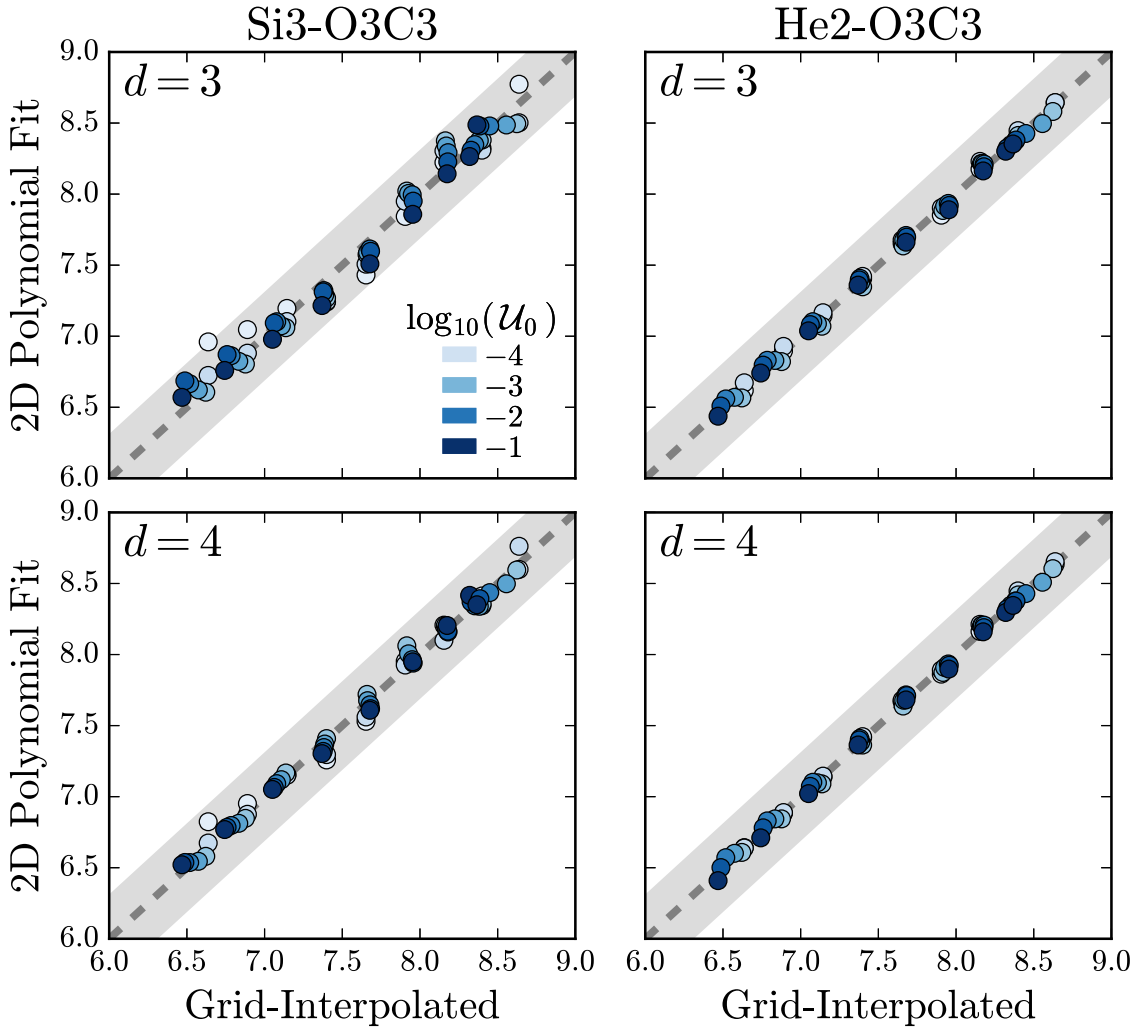


**Figure 6.** Comparison of oxygen abundances derived from the 2D polynomial fits ($y$-axis) and direct model grid interpolation ($x$-axis). The gray shaded region shows 0.3 dex scatter around a one-to-one relationship (dashed line). Left column: the Si3–O3C3 diagnostic, for the third-degree 2D polynomial (top; Equation (7) or Table 4) and the fourth-degree 2D polynomial (bottom; Equation (9) or Table 5). Right column: the He2–O3C3 diagnostic, for the degree = 3 2D polynomial (top; Equation (8) or Table 4) and the degree = 4 2D polynomial (bottom; Equation (9) or Table 5).

Moreover, the chemical composition of dust can evolve as grains lose atoms to the gas phase through high-energy processes that occur in the supernova-generated shock waves in the ISM. High-energy collisions between grains can cause erosion on the surface of dust, transferring elements (in particular Mg, Si, and Fe) from the grain surface to the gas phase. Notably, the fraction of silicon that is transferred back to the gas phase increases with shock velocity (see review on depletion patterns and dust evolution in Jones 2000).

Our model assumes that the gas-phase abundance of silicon scales with the oxygen abundance, and that a fixed fraction of silicon is depleted onto dust grains (Table 2), such that the ratio of between silicon and oxygen is constant in all models, $\log_{10}(\mathrm{Si/O}) = -1.9$. This is lower than the average $\log_{10}(\mathrm{Si/O}) = -1.6$ measured in extragalactic H II regions by Garnett et al. (1995) and the lensed galaxy from Berg et al. (2018), but similar to the $\log_{10}(\mathrm{Si/O}) = -1.8$ measured from the Steidel et al. (2016) stack of $z \sim 2$ galaxies.

A total of 21 of the 26 galaxies in the Berg sample have significant detections of the collisionally excited intercombination [Si III] $\lambda$1883,1892 doublet, which can be used to calculate the abundance of Si relative to C, and then combined with the C/O ratio to estimate the Si/O abundance ratio, as described in Berg et al. (2018). We note, however, that if the fraction of Si depleted onto dust grains varies significantly across the sample (i.e., if the depletion fraction varies with metallicity), the calculated Si/O ratios will be incorrect. A full analysis of Si/O abundances will be presented in D. Berg et al. (2020, in preparation).

In Figure 7, we again show the comparison between UV and optical metallicities for the Berg sample, derived using the Si3–O3C3 diagnostic. Now, each point is color-coded by $\log_{10}(\mathrm{Si/O})$. The four objects offset from the rest of the Berg et al. (2016, 2019) galaxies also have the largest $\log_{10}(\mathrm{Si/O})$ abundance ratios, between $-1.8 \leqslant \log_{10}(\mathrm{Si/O}) \leqslant -1.1$. The four objects (J171236, J132347, J025346, J092055) have an average silicon abundance of $\log_{10}(\mathrm{Si/O}) = -1.46 \pm 0.25$, which is more than 0.4 dex larger than the average silicon abundance of the full sample, $\log_{10}(\mathrm{Si/O}) = -1.89 \pm 0.48$, and the silicon abundance assumed in the model, $\log_{10}(\mathrm{Si/O}) = -1.9$. It is interesting to note that these four offset objects also show the best agreement between the UV and optical metallicities in the Si3–O3C3 diagnostic.

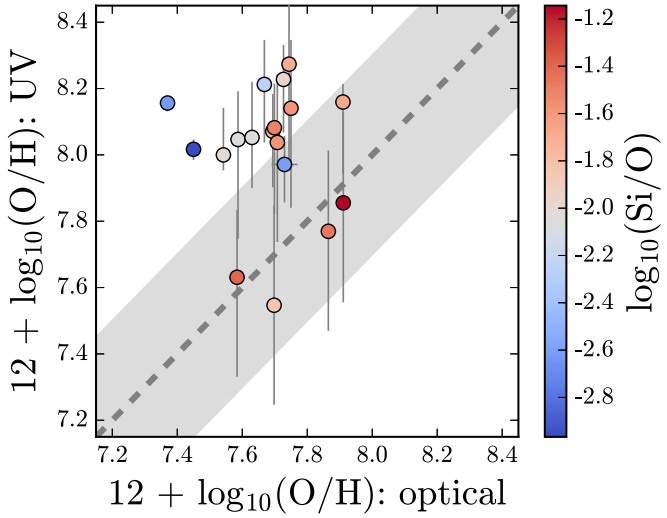


**Figure 7.** UV metallicities (*y*-axis), derived from the Si3–O3C3 diagnostic, compared to the optical metallicities (*x*-axis) for the Berg et al. (2016, 2019) galaxies. Objects are color-coded by $\log_{10}$(Si/O). We suggest that the large scatter in the metallicities derived with the Si3–O3C3 diagnostic is driven by variations in the gas-phase silicon abundance.

We conclude that the elevated Si/O abundance ratios in these four objects may be responsible for driving the large scatter in UV metallicities, though it is not clear what underlying physical process is responsible. If shocks driven by intense SF are responsible for returning additional silicon to the gas phase, we might expect the four offset objects to have larger ionization parameters or higher specific SFRs than the rest of the Berg sample, which they do not. The four objects have an average $\log_{10}\mathcal{U}_0 = -2.4 \pm 0.3$ and $\log_{10}$(sSFR) $= -8.1 \pm 0.2$, compared to the averages for the full sample of $\log_{10}\mathcal{U}_0 = -2.3 \pm 0.3$ and $\log_{10}$(sSFR) $= -8.1 \pm 0.3$.

Dust studies suggest that the amount of Si dust increases with reddening (e.g., Haris et al. 2016, but see also Mishra & Li 2017). We do not find a significant correlation between $E(B-V)$ and $\log_{10}$(Si/O) for these objects; however, the dust content in the BCD sample is generally quite low ($E(B-V) < 0.18$). A more in-depth investigation of gas-phase silicon abundances will be presented in future work.

### 6.2. Broad or Narrow Emission?

Thus far, we have assumed that the He II $\lambda$1640 and C IV $\lambda$1548,1551 emission is solely nebular in nature. However, He II $\lambda$1640 and C IV $\lambda$1548,1551 emission can also be produced in stellar photospheres, artificially inflating the measured nebular emission-line flux. In practice, it can be difficult to disentangle the narrow nebular and broad stellar components, especially at low S/N and moderate spectral resolution. Before discussing sources for the narrow, nebular emission, we briefly assess the level of "contamination" from stellar wind emission to the total line flux.

Stellar photospheric emission is produced in the winds of hot, young, stars. However, the C IV $\lambda$1548,1551 and He II $\lambda$1640 lines are produced in very different types of stars. We should thus expect that the stellar contribution for each of these lines will scale differently with stellar metallicity and operate on different timescales.

C IV is produced in the atmospheres of massive main-sequence stars, via line-driven winds. C IV emission is strongest at young ages (3–5 Myr and younger) and at high stellar metallicity (at or above solar metallicity; Walborn & Nichols-Bohlin 1987; Pauldrach et al. 1990; Leitherer et al. 1995; Walborn et al. 2002).

Current research suggests that only W-R stars or very massive stars (VMSs) should produce significant He II wind emission (e.g., Crowther et al. 2016; Leitherer et al. 2018). These stars are short-lived, and we do not expect them to dominate the He II emission in all but extremely young star bursts. He II emission from W-R stars should be strongest at later times (4–6 Myr) and at high stellar metallicity (e.g., Schaerer & Vacca 1998; Vink & de Koter 2005).

We note that our understanding of the physical mechanisms that drive the various W-R evolutionary pathways is still incomplete. Binary interactions enhance mass loss and provide additional pathways to strip the outer hydrogen envelope from a star (e.g., Eldridge et al. 2017). At low metallicities, rotational mixing can dredge up significant amounts of helium to the stellar surface, which can also produce broad He II emission (e.g., Yoon & Langer 2005; Cantiello et al. 2007; Eldridge et al. 2011, 2017; Choi et al. 2017). Recent theoretical work suggests that chemical dredge-up in hydrogen-burning main-sequence stars can produce surface enhancements in He and N consistent with W-R spectral classification (Roy et al. 2019).

In the MIST models, broad He II emission is produced by traditional W-R stars at high metallicity (solar like and above) and rotational mixing at low metallicity (10% solar and below; sometimes called quasi-homogeneous evolution or QHE). To quantify the relative importance of stellar and nebular emission for the C IV and He II spectral features, we calculate the flux from both the stellar and nebular components. We refer to this model as the `MIST+wind` model, which was first presented in B18. A full description of the process is found in B18; briefly, the "total" C IV or He II emission flux is calculated by summing the flux from both the broad and narrow emission components.

In Figure 8, we show the fraction of the total C IV flux (left) and He II flux (right) that is contained within the broad, stellar component ($F_{\rm broad}/F_{\rm total}$) as a function of model age, assuming $\log_{10}\mathcal{U}_0 = -2.5$. The lines are color-coded by metallicity, from $12 + \log_{10}$(O/H) $= 6.7$ ($\log_{10} Z/Z_\odot = -2$; purple) to $12 + \log_{10}$(O/H) $= 8.7$ ($\log_{10} Z/Z_\odot = 0$; orange). $F_{\rm broad}/F_{\rm total}$ initially increases as the population of young main-sequence stars builds. $F_{\rm broad}/F_{\rm total}$ eventually plateaus as the rate of stars being formed reaches an equilibrium with the rate of stars leaving the main sequence.

For both C IV and He II, $F_{\rm broad}/F_{\rm total}$ is highest in the solar metallicity models and decreases with decreasing metallicity. For C IV (left panel), stellar emission contributes $\sim$80% of the total C IV flux at solar metallicity, decreasing to 10% at $12 + \log_{10}$(O/H) $= 7.7$ (0.1 $Z_\odot$). For He II (right panel), stellar emission contributes $\sim$40% of the total He II flux at solar metallicity, and contributes less than a few percent of the total He II flux at $12 + \log_{10}$(O/H) $= 7.7$ (0.1 $Z_\odot$).

For both lines, the relative strength of the stellar emission at high metallicity is further enhanced by the paucity of narrow emission at these metallicities, a by-product of cooler nebular temperatures and softer radiation fields. Similarly, the broad contribution is more modest at low metallicities, partially driven by fewer traditional W-R stars (He II) and weaker line-driven winds (C IV). The narrow nebular emission is also

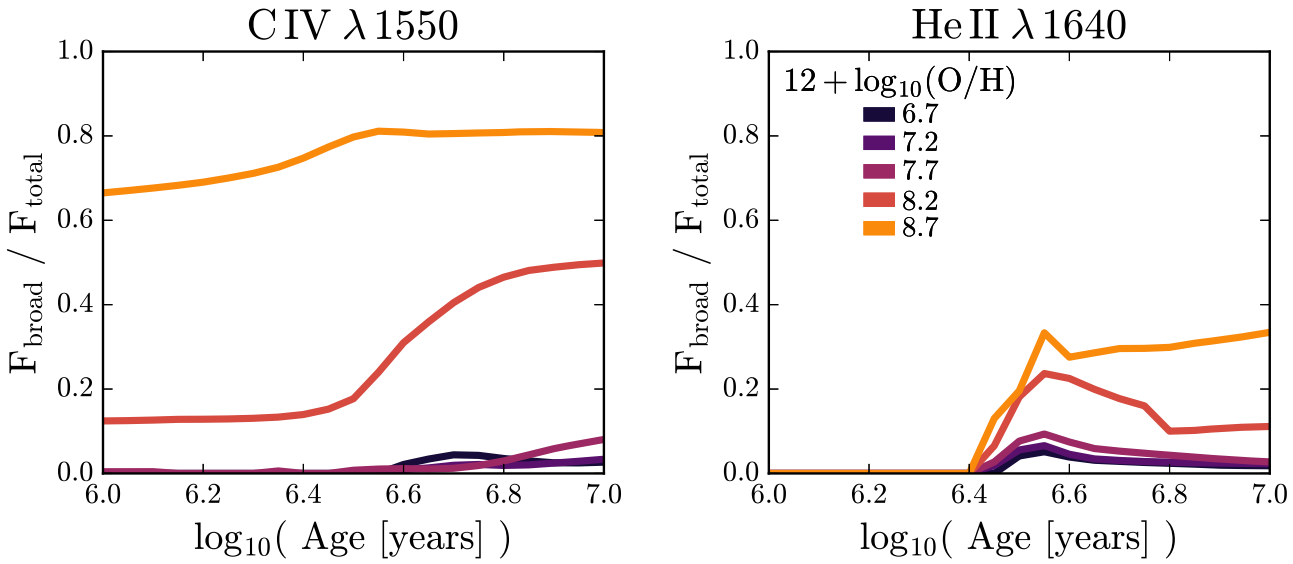


**Figure 8.** Left: the fraction of the total C IV flux (the sum of broad wind and narrow nebular) from the broad component as a function of time. Right: the fraction of the total He II flux (the sum of broad wind and narrow nebular) from the broad component as a function of time. In both panels, we use a constant-SFR model with $\log_{10}\mathcal{U}_0 = -2.5$. Lines are color-coded by metallicity, from $12 + \log_{10}(\mathrm{O/H}) = 6.7$ ($\log_{10}Z/Z_\odot = -2$; purple) to $12 + \log_{10}(\mathrm{O/H}) = 8.7$ ($\log_{10}Z/Z_\odot = 0$; orange).

stronger in these models, driven by higher nebular temperatures and harder radiation fields.

We note that the broad contribution to the total He II flux is difficult to interpret due to the brevity of the W-R phase, and will depend strongly on the SFH of the system. In star-bursting systems, the broad He II flux contribution from W-R stars can be as large as 80% at solar metallicity (B18). Thus, the CSFR models presented here represent one of the limiting SFH scenarios.

### 6.3. The Source of Narrow He II λ1640 Emission

Significant nebular He II emission requires high-energy photons, and current stellar models have difficulty producing the hard ionizing spectra required without invoking binary populations or rotating stars (e.g., Stark et al. 2014; Steidel et al. 2016; Byler et al. 2017; Choi et al. 2017). Harder ionizing spectra would produce stronger He II emission and create an extended partial ionization zone in the nebula, changing emission-line ratios.

We can test the sensitivity of the derived metallicities to the hardness of the ionizing spectrum using the `CloudyFSPS` model integrated within FSPS (Byler et al. 2017), which includes self-consistent nebular emission predictions for all isochrone sets available within FSPS: Padova, MIST, PARSEC, and BPASS. The nebular inputs (i.e., gas-phase abundances, geometry) are identical across all stellar models, which provides a clean test of the sensitivity of He II to the ionizing spectrum.[14] A comprehensive comparison of the hydrogen- and helium-ionizing properties of the MIST and BPASS models can be found in Choi et al. (2017).

We compare the UV diagnostic diagrams for the MIST model (which includes the effects of stellar rotation) and the BPASS model (which includes the effects of stellar multiplicity) in the top row of Figure 9 (left and center panels). The two model grids are similar in shape, but there are visible differences, especially at high metallicity ($8.0 \leqslant 12 + \log_{10}(\mathrm{O/H}) \leqslant 8.7$). At these metallicities, the harder ionizing spectra from the BPASS models produce more high-energy photons and relatively more He II emission, elevating the predicted He2C3 ratios.

The bottom row of Figure 9 shows the UV-derived metallicities ($y$-axis) compared to the optical metallicity ($x$-axis) for the MIST (left) and BPASS (center) models. Despite the use of harder ionizing spectra, the agreement between UV and optical metallicities has not noticeably improved. With the MIST models, 11 of the 24 galaxies (46%) have UV metallicities that agree with optical metallicities, within error. For the BPASS models, that number is increased to 12 (50%).

To understand the scatter between UV and optical metallicities, we calculate the average offset of the data points from a one-to-one relationship and the percentage of galaxies that fall within 0.3 dex of the one-to-one relationship, shown by the gray shaded region in Figure 9. As discussed earlier, ±0.3 dex represents the typical systematic errors inherent in optical strong-line methods.

For the MIST models, the UV metallicities show an average offset of $0.11 \pm 0.24$ dex from the optical, while 65% of the galaxies fall within 0.3 dex of the gray dashed line with slope unity. For the BPASS models, the UV metallicities have an average offset of $-0.12 \pm 0.30$ dex, and 60% of the galaxies fall within 0.3 dex of the gray dashed line with slope unity.

Thus, we do not find any statistically significant improvement in the offset or scatter of the UV metallicities with the BPASS models. We note that the use of harder ionizing spectra does not improve metallicity estimates for the MEGaSaURA galaxies (green squares).

The right column of Figure 9 shows the `MIST+wind` grid (top) and the resulting UV–optical metallicity comparison (bottom). The inclusion of stellar He II emission in the `MIST+wind` grid increases the model He2C3 ratios by 0.1–0.3 dex ($y$-axis) at metallicities above $12 + \log_{10}(\mathrm{O/H}) = 8$.

When the metallicity is calculated from the `MIST+wind` grid and compared to the metallicity derived from optical emission lines (bottom right panel), the agreement between

[14] We compare the MIST and BPASS models using models with a constant SFR. To ensure that we are comparing truly "equilibrated" populations, we assume a constant SFR over 10 Myr for the MIST models and 100 Myr for the BPASS models, as suggested by Xiao et al. (2018).

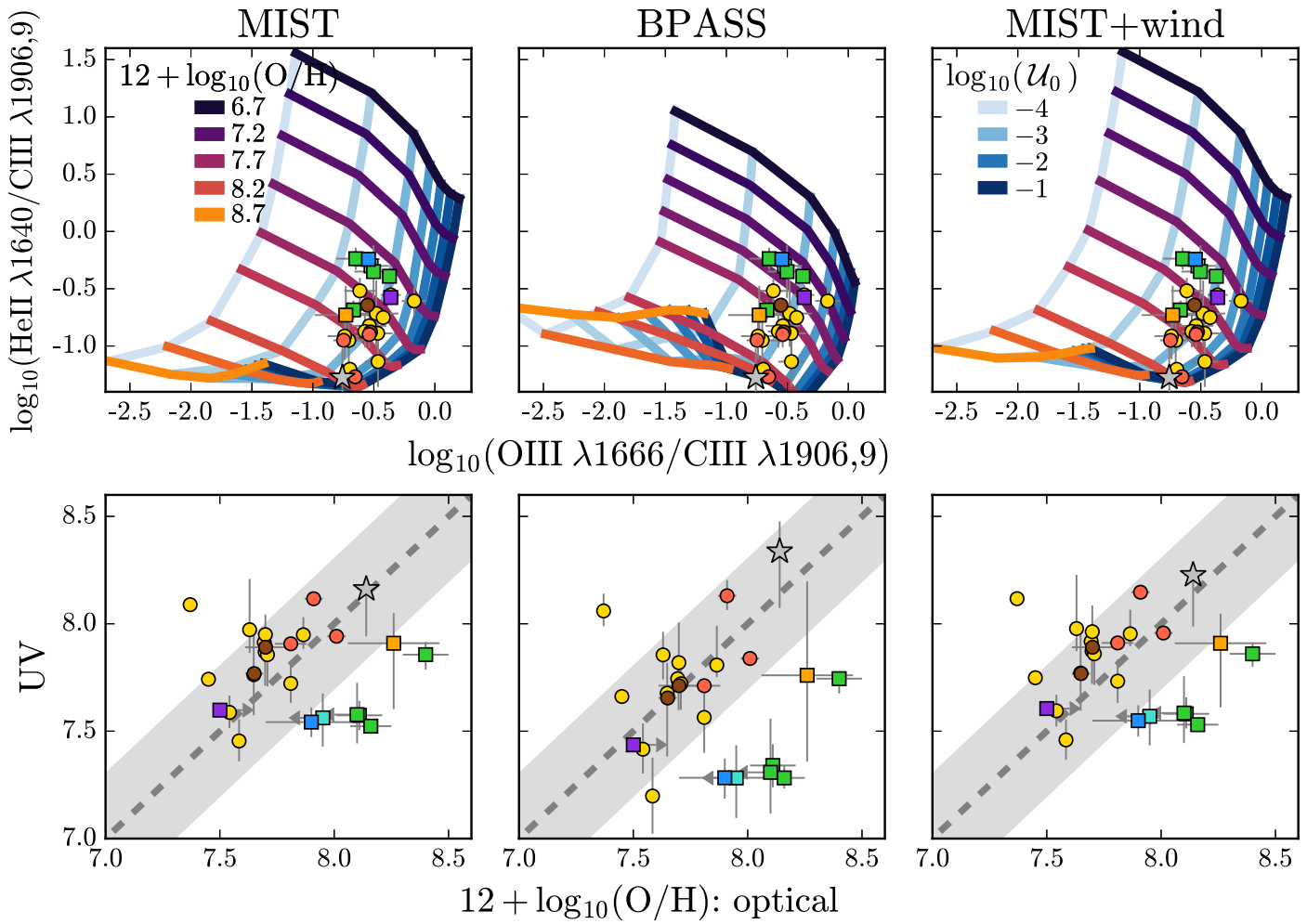


**Figure 9.** Top row: He2–O3C3 diagnostic diagrams using the MIST (left), BPASS (center), and `MIST+wind` (right) stellar models. Bottom row: UV metallicities (*y*-axis) derived from the He2–O3C3 diagnostic compared to the optical oxygen abundance (*x*-axis) for models using the MIST (left), BPASS (center), and `MIST+wind` (right) stellar models. The harder ionizing spectra from the BPASS models do not significantly improve the agreement between UV and optical metallicities. Some objects show clear improvement with either the BPASS or `MIST+wind` models.

UV- and optically derived metallicities is not noticeably improved. The `wind` grid shows a mean offset of $0.1 \pm 0.23$, statistically indistinguishable from the MIST grid. We also note that the use of the `wind` grid does not improve UV metallicity estimates for the MEGaSaURA galaxies (green squares), which are still more than 0.8 dex smaller than those derived using optical emission lines.

Despite the complications associated with modeling He II, the He2–O3C3 diagnostic yields metallicity measurements that agree well with optical measurements, especially at low metallicities ($12 + \log_{10}(O/H) \lesssim 8$). However, on a galaxy by galaxy basis, improvement between UV and optical metallicities changes whether the BPASS models or the `MIST+wind` models are used. Put differently, some objects are better fit with the BPASS models, while other objects are better fit with the `MIST+wind` models. This could indicate that multiple competing processes are at work, impacting the observed He II fluxes. Separating and characterizing these different processes will likely require a joint analysis of ISM properties and the local massive star populations in these objects.

### *6.4. The Source of Narrow C IVλ1550 Emission*

Similar to He II, C IV is a relatively high-excitation line. As in the previous section, we repeat the experiment with the MIST and BPASS models for the C4–O3C3 diagnostic to determine if a harder radiation field can improve the disagreement between model and observed C IV strengths.

Figure 10 shows the resulting MIST (left), BPASS (center), and `MIST+wind` (right) comparisons. The harder ionizing spectra found in the BPASS models produce larger C4O3 ratios, showing clear improvement when compared to observed C4O3 ratios, and the BPASS grid is able to reproduce most of the observed line ratios, with the exception of one of the Senchyna et al. (2017) galaxies (red circle). It is thus unsurprising that the metallicities derived using the BPASS models show a clear improvement over the MIST models. The galaxies with UV metallicities that agree with optical estimates increases from 8% (MIST) to 17% (BPASS). While both grids still overestimate the UV metallicity, the offset is decreased with the BPASS models. For the MIST models, the average offset is $0.57 \pm 0.3$ dex. This offset is decreased to $0.24 \pm 0.4$ with the BPASS models.

The right column of Figure 10 shows the `MIST+wind` grid (top) and the resulting UV–optical metallicity comparison

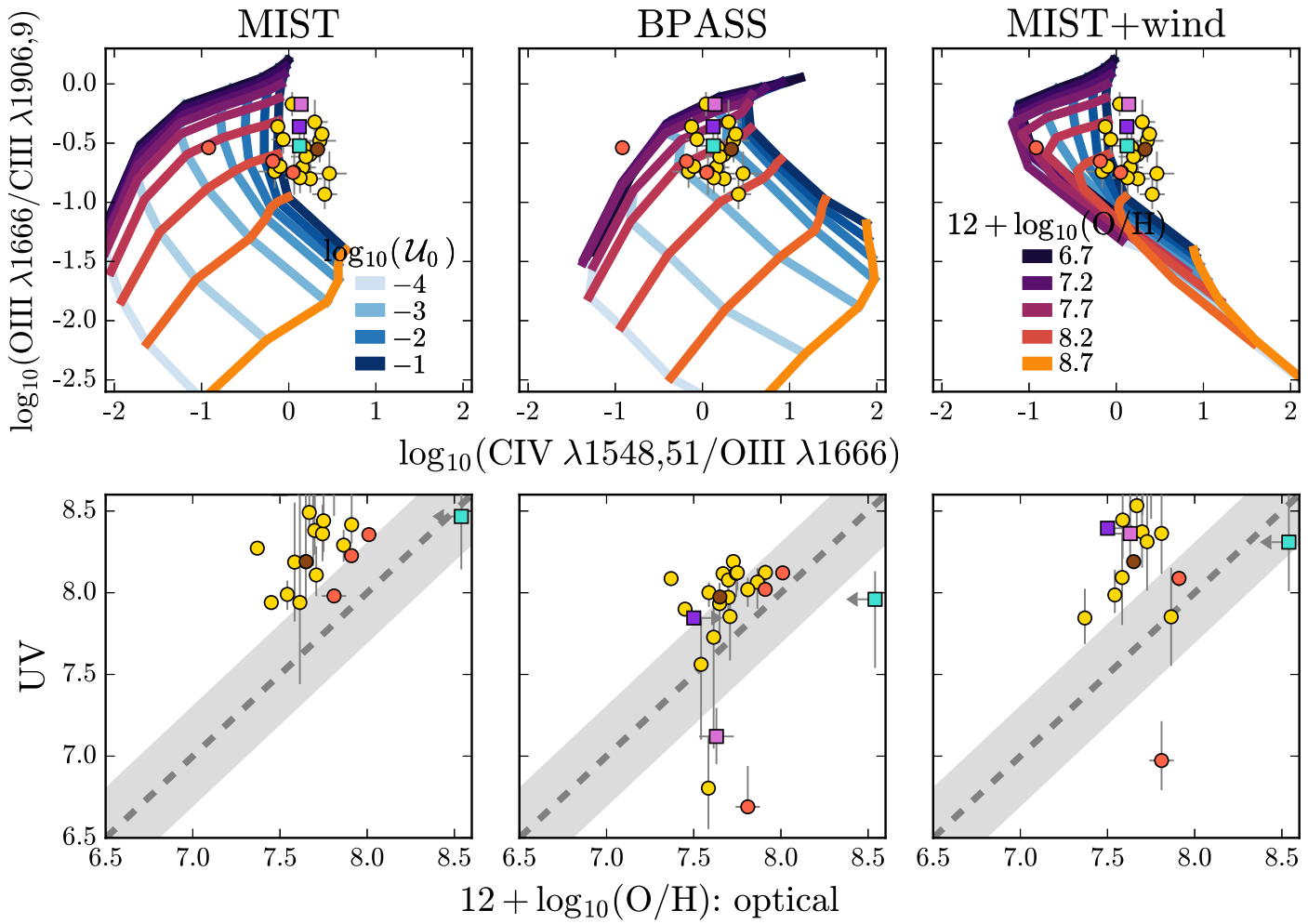


**Figure 10.** Top row: C4–O3C3 diagnostic diagrams using the MIST (left), BPASS (center), and `MIST+wind` (right) stellar models. Bottom row: UV metallicities (*y*-axis) derived from the He2–O3C3 diagnostic compared to the optical oxygen abundance (*x*-axis) for models using the MIST (left), BPASS (center), and `MIST+wind` (right) stellar models. The harder ionizing spectra from the BPASS models significantly improve the agreement between UV and optical oxygen abundance.

(bottom). Model C4O3 ratios increase when stellar emission is included in the model, especially for models at high metallicity and low ionization parameters. The agreement between model grid and data is still poor, and unsurprisingly, the agreement between UV and optical metallicities shows little improvement over the standard MIST model. The UV metallicities are still larger than those in the optical, with an average offset of $0.62 \pm 0.5$.

The lack of improvement with the `MIST+wind` grid does not imply that wind contamination cannot be responsible for inflating measured C IV fluxes, rather that the stellar emission as implemented in this model does not improve metallicity constraints. We note that wind predictions vary substantially from model to model and are poorly constrained at low metallicity.

Clearly, there is still work to be done to fully understand C IV emission from galaxies, locally and at high redshift. The BPASS grid provides an improved interpretation of C IV line strengths, but still does not reproduce the full range of observed C4O3 line ratios. Moreover, none of the C IV grids show a positive correlation between UV and optical metallicity. Caution should be used when interpreting C IV line strengths, especially at high redshift, where different ISM conditions may prevail.

### 6.5. C/O Variations

The B18 model uses a polynomial equation to describe the increase of [N/H] with [O/H] and [C/H] with [O/H] (Section 2.2). The relationship accounts for the additional production of N and C at high metallicity and is matched to observations of local star-forming galaxies. These empirical relationships are used to describe the broad behavior of the galaxy population, but individual objects can have abundance patterns for C, N, and O that deviate from these relationships.

The C/O relationship used in this work was derived to match the Berg et al. (2016, 2019) galaxies, and as such, most of the galaxies in the Berg sample have C/O ratios that are well matched to our model. However, there are a handful of objects with C/O ratios that deviate significantly from our C/O relationship. It is possible that the C III] line strengths are too sensitive to the specific C and O abundances to be a useful metallicity indicator. Pérez-Montero & Amorín (2017) presented an analysis of metallicities derived using C III] lines and found that it was essential to estimate the C/O ratio before calculating the metallicity.

The emissivity of [O III] $\lambda$1666 is much more sensitive to $T_e$ (and thus the gas-phase oxygen abundance) than the emissivity of C III] $\lambda$1909. However, photoionization models have shown that C III] line strengths are more sensitive to $T_e$ (and thus the

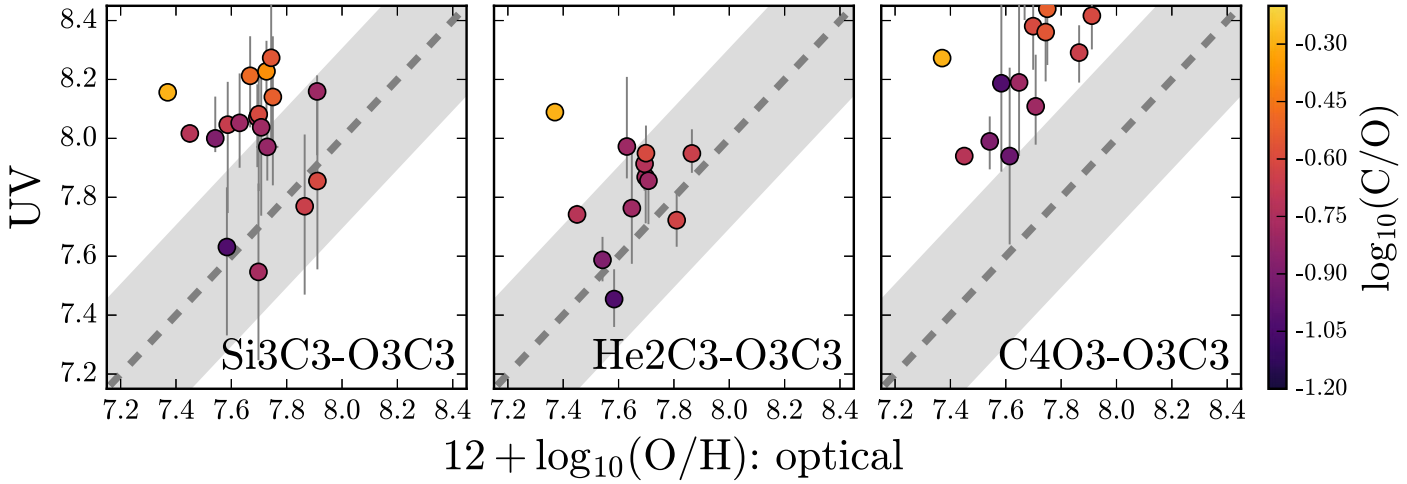


**Figure 11.** Comparison between UV metallicity (*y*-axis) and optical metallicity (*x*-axis) for the Berg et al. (2016, 2019) galaxies, using the Si3–O3C3 diagnostic (left), He2–O3C3 diagnostic (middle), and C4–O3C3 diagnostic (right). Objects are color-coded by the measured C/O ratio. While the UV metallicity is weakly correlated with the C/O ratio, variations in C and O abundances alone cannot be responsible for driving the large scatter in UV metallicities.

gas-phase oxygen abundance) than to the absolute gas-phase carbon abundance (Jaskot & Ravindranath 2016; Byler et al. 2018). Put differently, C III] line strengths vary more strongly with changes to the gas-phase oxygen abundance than with changes to the gas-phase C/O ratio. As such, to first order, both the [O III] and C III] emission lines trace the gas-phase oxygen abundance.

In Figure 11, we show the comparison between UV and optical metallicities for the Berg sample, for the Si3–O3C3 diagnostic (left), He2–O3C3 diagnostic (middle), and C4–O3C3 diagnostic (right). In all panels, the points are color-coded by C/O ratio. There is a weak trend between C/O and UV metallicity, where larger C/O ratios are found in higher-metallicity objects. For two objects with identical optical metallicities but a factor of 3 difference in C/O ratio, the difference in derived UV metallicity is less than 0.1 dex, which is smaller than the statistical errors calculated here. This suggests that metallicities derived from the C III] $\lambda$1906,1909 and [O III] $\lambda$1661,1666 lines will not be dominated by uncertainties driven by C/O variations.

Despite recent progress in building samples of objects with rest-UV and rest-optical spectra, there is still much work to be done to interpret rest-frame UV spectra. In particular, it is critical that we understand the behavior of UV emission lines in the context of optically derived ISM properties so that we can fully harness their diagnostic power in preparation for JWST.

## 7. Conclusions

We have derived gas-phase oxygen abundances for galaxies with rest-UV spectra using different combinations of UV emission lines (Table 3). For a sample of galaxies with both rest-UV and rest-optical spectra, we have compared UV and optical abundances to identify useful UV metallicity diagnostics. Our conclusions are as follows.

1. Metallicities derived using the [Si III] $\lambda$1893 emission line do not reliably correlate with optical metallicities and show a comparatively large scatter, with an average offset of $0.35 \pm 0.28$ dex from the optical (Figure 3). We suggest that this is likely driven by variations in the silicon abundance relative to oxygen, either from variable dust depletion factors or from enhanced silicon abundances in the gas phase caused by the erosion of Si from the surface of dust grains by shocks (Figure 7).
2. UV diagnostics that include the He II $\lambda$1640 emission line are reliable metallicity indicators at metallicities below $12 + \log_{10}(\mathrm{O/H}) \sim 8$. At higher metallicities ($12 + \log_{10}(\mathrm{O/H}) \sim 8.5$), discrepant abundances may arise due to contamination by stellar He II emission (Figure 4). Consistent gas-phase abundances are found regardless of stellar model choice (rotating or binary; Figure 9), with an average offset of $0.11 \pm 0.24$ dex for the rotating MIST models and $-0.12 \pm 0.30$ dex for the binary BPASS models.
3. UV diagnostics that include the C IV $\lambda$ 1548,1550 emission lines are unreliable metallicity indicators. None of the models tested in this work showed a positive correlation between UV and optical metallicity when the C IV diagnostic was used. The harder radiation fields found in the BPASS models significantly improve agreement between the model and observed C4O3 line ratios, reducing the offset between UV and optical metallicities by 0.3 dex. The C4–O3C3 abundances are still offset from optical abundances by 0.2 dex, even with the BPASS models, which suggests that stellar models do not produce hard-enough ionizing spectra. Some of the remaining offset may be driven by contamination from stellar emission, though our interpretation is further complicated by strong interstellar absorption just blueward of the emission feature, which could complicate continuum estimation in low-resolution, low-S/N observations (Figure 5). We note that the disagreement could also be driven by contamination from shocks or AGNs in some cases, as C IV is also sensitive to these power sources.
4. We provide new oxygen abundance diagnostics for the Si3–O3C3 and He2–O3C3 diagrams based on polynomial fits to the model grid surface (Section 5.4). These fits are valid for $6.2 \leqslant 12 + \log_{10}(\mathrm{O/H}) \leqslant 9.2$, and $-4.0 \leqslant \log_{10}\mathcal{U}_0 \leqslant -1.0$.
5. We calculate the relative flux from stellar and nebular emission for the He II and C IV spectral features for the constant-SFR models used in this work. For C IV, at high metallicities ($12 + \log_{10}(\mathrm{O/H}) > 8.2$), the broad stellar

emission contributes more than 50% of the total emission flux. However, at low metallicities ($12 + \log_{10}(\mathrm{O/H}) \leqslant 8$), stellar emission contributes at most 10%–20% of the total C IV flux (Figure 8). Compared to the stellar C IV emission, the flux contribution from stellar He II emission is smaller (at most 40% of the total flux), because in the models used in this work, the broad He II emission is produced by short-lived W-R stars.

6. In Appendix B, we calculate direct-$T_e$ oxygen abundances for our photoionization models using the UV [O II] $\lambda$2471, [O II] $\lambda$3729, [O III] $\lambda$1666, and [O III] $\lambda$2321 emission lines. We compare the UV direct-$T_e$ abundances with optical direct-$T_e$ abundances and find that the two abundances are tightly correlated. The UV direct-$T_e$ abundances are systematically 0.1 dex lower than the optical direct-$T_e$ abundances, driven by temperature differences, as the UV emission lines are higher excitation transitions.

Currently planned studies of $z > 6$ galaxies with NIRSpec on JWST will rely on UV emission-line diagnostics to calculate metallicities. Obtaining rest-optical [N II]/H$\alpha$ measurements with MIRI for even a small subset of these objects will be expensive, without NIRSpec's multiplexing ability. For those objects observed with NIRSpec and MIRI, our results suggest that metallicities calculated from NIRSPec will be quite low ($6.5 \lesssim 12 + \log_{10}(\mathrm{O/H}) \lesssim 7.5$), while metallicities calculated from MIRI will be moderately high ($7.5 \lesssim 12 + \log_{10}(\mathrm{O/H}) \lesssim 8.5$).

While the proposed UV metallicity diagnostics show theoretical promise, in practice, UV-derived abundances show considerable scatter and do not always recover optical abundances. Unfortunately, the combination of fragmented wavelength coverage and the inhomogeneous sample selection makes it difficult to determine the source of the discrepancy. A first step in understanding these diagnostics requires a detailed comparison of gas properties in a small set of galaxies with high-S/N, high-resolution, aperture-matched rest-frame UV and optical spectroscopy. With these observations, we can detect the faint auroral emission lines and ensure the identification of stellar and shock emission, if present, and quantify the relationship between UV and optical measures of temperature, density, ionization parameter, and C, N, O, and Si abundances. As it stands, the current discrepancies between UV and optical diagnostics critically limit our ability to study chemical enrichment across cosmic time.

We would like to thank the anonymous referee for thorough and constructive feedback that greatly improved this work. Parts of this research were supported by the Australian Research Council Centre of Excellence for All Sky Astrophysics in 3 Dimensions (ASTRO 3D), through project number CE170100013. L.J.K. gratefully acknowledges the support of an ARC Laureate Fellowship (FL150100113). This research has made use of NASA's Astrophysics Data System Bibliographic Services. This research made use of Astropy,[15] a community-developed core Python package for Astronomy (Astropy Collaboration et al. 2013; Price-Whelan et al. 2018).

[15] http://www.astropy.org

**Table A1**
Polynomial Fits to the Oxygen Abundance Offset between CLOUDY and the Direct-$T_e$ Method

| SFH | Age (Myr) | $\log_{10}\mathcal{U}_0$ | $a$ | $b$ | $c$ | $d$ |
|---|---|---|---|---|---|---|
| CSFR | 10 | −4.0 | −0.01 | 0.30 | −1.15 | 5.09 |
| | | −3.5 | −0.03 | 0.75 | −4.48 | 13.10 |
| | | −3.0 | −0.09 | 2.06 | −13.97 | 35.98 |
| | | −2.5 | −0.18 | 4.02 | −28.25 | 70.38 |
| | | −2.0 | −0.22 | 4.90 | −34.60 | 85.52 |
| | | −1.5 | −0.23 | 5.11 | −36.14 | 89.13 |
| | | −1.0 | −0.23 | 5.14 | −36.38 | 89.78 |
| Burst | 1 | −4.0 | −0.01 | 0.31 | −1.23 | 5.32 |
| | | −3.5 | −0.03 | 0.71 | −4.16 | 12.36 |
| | | −3.0 | −0.08 | 1.83 | −12.33 | 32.02 |
| | | −2.5 | −0.17 | 3.67 | −25.70 | 64.24 |
| | | −2.0 | −0.22 | 4.75 | −33.58 | 83.17 |
| | | −1.5 | −0.23 | 5.06 | −35.81 | 88.47 |
| | | −1.0 | −0.23 | 5.09 | −36.06 | 89.14 |
| Burst | 2 | −4.0 | −0.01 | 0.31 | −1.23 | 5.31 |
| | | −3.5 | −0.03 | 0.75 | −4.48 | 13.12 |
| | | −3.0 | −0.09 | 1.96 | −13.25 | 34.28 |
| | | −2.5 | −0.17 | 3.80 | −26.68 | 66.63 |
| | | −2.0 | −0.21 | 4.63 | −32.69 | 80.97 |
| | | −1.5 | −0.22 | 4.79 | −33.81 | 83.56 |
| | | −1.0 | −0.22 | 4.79 | −33.81 | 83.62 |
| Burst | 3 | −4.0 | −0.01 | 0.25 | −0.79 | 4.22 |
| | | −3.5 | −0.03 | 0.75 | −4.44 | 13.04 |
| | | −3.0 | −0.08 | 1.77 | −11.91 | 31.07 |
| | | −2.5 | −0.13 | 2.82 | −19.55 | 49.41 |
| | | −2.0 | −0.18 | 3.92 | −27.54 | 68.61 |
| | | −1.5 | −0.20 | 4.43 | −31.18 | 77.27 |
| | | −1.0 | −0.21 | 4.59 | −32.39 | 80.21 |
| Burst | 4 | −4.0 | −0.02 | 0.39 | −1.81 | 6.66 |
| | | −3.5 | −0.05 | 1.11 | −7.04 | 19.26 |
| | | −3.0 | −0.13 | 2.78 | −19.23 | 48.63 |
| | | −2.5 | −0.19 | 4.27 | −30.04 | 74.46 |
| | | −2.0 | −0.24 | 5.34 | −37.71 | 92.78 |
| | | −1.5 | −0.27 | 5.98 | −42.41 | 104.08 |
| | | −1.0 | −0.29 | 6.27 | −44.51 | 109.22 |
| Burst | 5 | −4.0 | −0.03 | 0.61 | −3.44 | 10.55 |
| | | −3.5 | −0.08 | 1.68 | −11.21 | 29.32 |
| | | −3.0 | −0.14 | 3.05 | −21.21 | 53.44 |
| | | −2.5 | −0.19 | 4.24 | −29.85 | 74.18 |
| | | −2.0 | 0.00 | 0.03 | 0.25 | 2.05 |
| | | −1.5 | 0.00 | 0.03 | 0.25 | 2.04 |
| | | −1.0 | 0.00 | 0.03 | 0.25 | 2.04 |

**Note.** Fits are of the form $y = ax^3 + bx^2 + cx + d$, where $y \equiv 12 + \log_{10}(\mathrm{O/H})$ (CLOUDY) and $x \equiv 12 + \log_{10}(\mathrm{O/H})$ (direct-$T_e$).

## Appendix A
## Polynomial Fits to Offset between Theoretical and Measured Oxygen Abundances

Table A1 includes the coefficients for the third-order polynomial used to fit the CLOUDY and direct-$T_e$ method oxygen abundances. The fits are computed for both CSFR and instantaneous burst models at each ionization parameter. Table A2 includes the coefficients for the linear function used to fit the CLOUDY and PP04-N2 method oxygen abundances. As before, fits are computed for both CSFR and instantaneous burst models at each ionization parameter.

For three objects in the sample, we were unable to calculate direct-$T_e$ or PP04-N2 oxygen abundances, and instead used the KK04-R23 method. Table A3 includes the third-order polynomial used to fit the CLOUDY and KK04-R23 oxygen

**Table A2**
Polynomial Fits to the Oxygen Abundance Offset between CLOUDY and the PP04-N2 Method

| SFH | Age (Myr) | $\log_{10}\mathcal{U}_0$ | $a$ | $b$ |
|---|---|---|---|---|
| CSFR | 10 | −4.0 | 0.53 | 4.00 |
| | | −3.5 | 0.52 | 4.00 |
| | | −3.0 | 0.53 | 3.81 |
| | | −2.5 | 0.54 | 3.61 |
| | | −2.0 | 0.55 | 3.46 |
| | | −1.5 | 0.55 | 3.31 |
| | | −1.0 | 0.56 | 3.15 |
| Burst | 1 | −4.0 | 0.54 | 3.90 |
| | | −3.5 | 0.54 | 3.91 |
| | | −3.0 | 0.54 | 3.75 |
| | | −2.5 | 0.55 | 3.58 |
| | | −2.0 | 0.55 | 3.46 |
| | | −1.5 | 0.55 | 3.34 |
| | | −1.0 | 0.56 | 3.21 |
| Burst | 2 | −4.0 | 0.53 | 3.98 |
| | | −3.5 | 0.53 | 3.98 |
| | | −3.0 | 0.54 | 3.79 |
| | | −2.5 | 0.54 | 3.59 |
| | | −2.0 | 0.55 | 3.43 |
| | | −1.5 | 0.56 | 3.29 |
| | | −1.0 | 0.57 | 3.13 |
| Burst | 3 | −4.0 | 0.51 | 4.15 |
| | | −3.5 | 0.51 | 4.09 |
| | | −3.0 | 0.53 | 3.82 |
| | | −2.5 | 0.55 | 3.56 |
| | | −2.0 | 0.56 | 3.39 |
| | | −1.5 | 0.57 | 3.22 |
| | | −1.0 | 0.58 | 3.03 |
| Burst | 4 | −4.0 | 0.51 | 4.08 |
| | | −3.5 | 0.51 | 4.07 |
| | | −3.0 | 0.52 | 3.88 |
| | | −2.5 | 0.53 | 3.68 |
| | | −2.0 | 0.53 | 3.55 |
| | | −1.5 | 0.54 | 3.44 |
| | | −1.0 | 0.54 | 3.30 |
| Burst | 5 | −4.0 | 0.40 | 4.87 |
| | | −3.5 | 0.42 | 4.71 |
| | | −3.0 | 0.47 | 4.27 |
| | | −2.5 | 0.51 | 3.83 |
| | | −2.0 | 0.54 | 3.52 |
| | | −1.5 | 0.56 | 3.28 |
| | | −1.0 | 0.59 | 3.04 |

**Note.** Fits are of the form $y = ax + b$, where $y \equiv 12 + \log_{10}(\mathrm{O/H})$ (CLOUDY) and $x \equiv 12 + \log_{10}(\mathrm{O/H})$ (PP04-N2).

abundances. The fits are computed for a 10 Myr CSFR model at each ionization parameter.

## Appendix B
## Comparison of UV and Optical Direct-$T_e$ Abundances

We have already discussed the established practice for determining direct-$T_e$ abundances using emission lines in the optical part of the spectrum. Here, we briefly explore comparable measurements using emission lines in the UV.

The direct-temperature method relies on the use of collisionally excited transitions with a difference in energy of order $\sim kT_e$. The two transitions are populated by electron–ion collisions, and the relative population in each energy level will thus depend directly on the electron temperature of the gas. In the optical, the temperature leverage comes from the combination of the $^1S_0$ to $^1D_2$ transition ($\lambda$4363) and the $^1D_2$ to $^3P_2$ ($\lambda$5007) transition (often with the addition of the $^1D_2$ to $^3P_1$ transition at $\lambda$4959).

**Table A3**
Polynomial Fits to the Oxygen Abundance Offset between CLOUDY and the KK04-R23 Method (Upper and Lower Branches, Respectively)

| SFH | Age (Myr) | log $U$ | $a$ | $b$ | $c$ | $d$ |
|---|---|---|---|---|---|---|
| CSFR | 10 | −4.0 | −0.13 | 2.93 | −20.80 | 54.22 |
| | | −3.5 | −0.23 | 5.33 | −39.97 | 105.36 |
| | | −3.0 | −0.41 | 9.44 | −71.22 | 184.30 |
| | | −2.5 | −0.61 | 13.92 | −104.75 | 267.70 |
| | | −2.0 | −0.78 | 17.70 | −132.93 | 337.41 |
| | | −1.5 | −0.91 | 20.74 | −155.59 | 393.48 |
| | | −1.0 | −1.04 | 23.46 | −175.90 | 443.74 |
| CSFR | 10 | −4.0 | −1.76 | 47.32 | −421.84 | 1259.10 |
| | | −3.5 | −1.39 | 37.30 | −331.78 | 989.16 |
| | | −3.0 | 0.03 | −0.42 | 0.75 | 12.31 |
| | | −2.5 | 2.05 | −53.56 | 467.45 | −1353.25 |
| | | −2.0 | 3.87 | −101.48 | 886.79 | −2575.71 |
| | | −1.5 | 5.45 | −142.88 | 1248.10 | −3626.04 |
| | | −1.0 | 6.85 | −179.54 | 1567.75 | −4554.40 |

**Note.** Fits are of the form $y = ax^3 + bx^2 + cx + d$, where $y \equiv 12 + \log_{10}(\mathrm{O/H})$ (CLOUDY) and $x \equiv 12 + \log_{10}(\mathrm{O/H})$ (KK04-R23).

Similar transitions exist in the UV wavelength regime, making it possible to derive direct-method metallicities using only UV emission lines. For the $O^{++}$ zone, the temperature leverage comes from the combination of the $^5S_2 \rightarrow {}^3P_2$ ($\lambda$1666) and the $^1S_0 \rightarrow {}^3P_1$ ($\lambda$2321) transitions. For the $O^+$ zone, the temperature-sensitive transitions are the $^2P_{1/2} \rightarrow {}^4S_{3/2}$ ($\lambda$2471) and the $^2D_{3/2} \rightarrow {}^4S_{3/2}$ ($\lambda$3727) transitions. It is worth noting that the the [O II] $\lambda$2471 and [O III] $\lambda$2321 lines are very weak and have only been detected in a handful of galaxies; [O II] $\lambda$2471 is ∼6% of the [O II] $\lambda$3727 line strength while [O III] $\lambda$2321 is ∼2% of the [O III] $\lambda$4959 line strength.

To follow the methodology used in the optical, we must find temperatures and densities for the $O^+$ and $O^{++}$ zones. While there are a number of density-sensitive line combinations in the UV, the brightest line combinations (C III]$\lambda$1906,1909 and [Si III]$\lambda$1883,1892) are not sensitive to densities below $\sim 10^3$ cm$^{-3}$ (Berg et al. 2019). We instead assume a constant $n_e = 100$ cm$^{-3}$, which is the density used in the CLOUDY models.[16]

The temperature of the $O^+$ zone is calculated using the ([O II] $\lambda$2471)/([O II] $\lambda$ 3727 + [O II] $\lambda$ 3729) ratio. The ionic abundance for $O^+$ is calculated with `PyNeb` using

$$\left[\frac{\mathrm{O}^{++}}{\mathrm{H}^+}\right] = \frac{I\ \lambda2471 + I\ \lambda3727 + I\ \lambda3729}{I\ \mathrm{H}\beta} \cdot \frac{j_{\mathrm{H}\beta}}{j_\lambda}. \quad \text{(B1)}$$

The temperature of the $O^{++}$ zone is calculated using the [O III] $\lambda$1666/[O III] $\lambda$2321 ratio. The total ionic abundance for

[16] The use of densities calculated from C III] and [Si III] ratios changes the resultant oxygen abundances by less than 0.1 dex and is thus not a significant source of error.

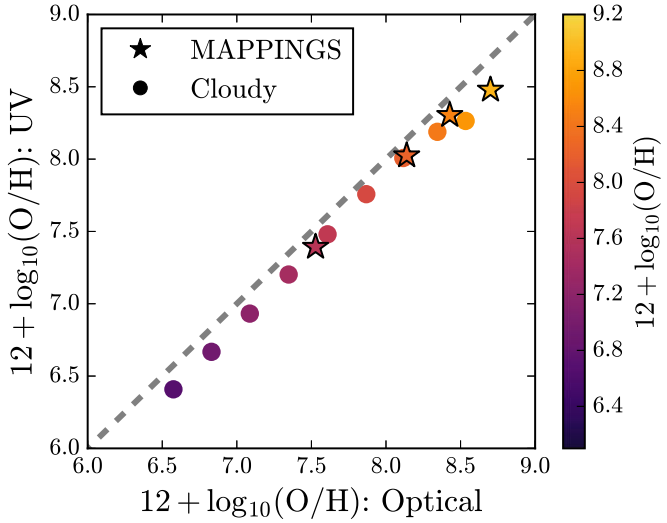


**Figure B1.** Comparison of direct-$T_e$ metallicities using optical emission lines ($x$-axis) and UV emission lines ($y$-axis). Circular markers show predictions from the CLOUDY photoionization model used in this work, while star-shaped markers show predictions from the MAPPINGS photoionization code (Kewley et al. 2019a). Color indicates the input gas-phase oxygen abundance, and the black dashed line shows a one-to-one relationship. Direct-$T_e$ abundances using UV and optical emission lines are correlated, but the UV-derived abundances are systematically lower than the optically derived abundances by ∼0.2 dex.

$O^{++}$ is calculated with `PyNeb` using

$$\left[\frac{O^+}{H^+}\right] = \frac{I\ \lambda1666 + I\ \lambda2321}{I\ H\beta} \cdot \frac{j_{H\beta}}{j_\lambda}. \quad \text{(B2)}$$

The total oxygen abundance is then calculated as the sum of the ionic abundances

$$\log_{10}(O/H) = \left[\frac{O^{++}}{H^+}\right] + \left[\frac{O^+}{H^+}\right], \quad \text{(B3)}$$

again, assuming a negligible contribution from $O^{+++}$ ions.

In Figure B1, we show direct-temperature metallicities from optical emission lines ($x$-axis) and UV emission lines ($y$-axis) from two different photoionization models, CLOUDY (circles; Byler et al. 2018) and MAPPINGS (squares; Kewley et al. 2019a). The UV and optical abundances are correlated, and the two different photoionization models produce very similar predictions for both UV and optical metallicities. However, the UV direct-$T_e$ abundances are systematically lower than the optical direct-$T_e$ abundances by ∼0.2 dex. This offset is likely driven by temperature differences in the UV and optical direct-$T_e$ calculation; the oxygen lines in the UV are higher energy transitions and are produced in the inner regions of the nebula where temperatures are higher.

We note that the [O II] λ2471 and [O III] λ2321 lines are quite weak and difficult to observe, and thus large samples of direct-method metallicities in the UV are unlikely. Unfortunately, the weak [O II] λ2471 and [O III] λ2321 lines are the only oxygen-based temperature anchors in the UV. For objects with both rest-UV and rest-optical spectroscopy, it is common to combine the [O III] λ1661,1666 with the optical [O III] λ5007,4959 lines for temperature determinations. Combining UV and optical emission lines introduces additional uncertainties, with flux calibration and aperture matching between UV and optical observations.

## ORCID iDs

Nell Byler https://orcid.org/0000-0002-7392-3637
Lisa J. Kewley https://orcid.org/0000-0001-8152-3943
Jane R. Rigby https://orcid.org/0000-0002-7627-6551
Danielle A. Berg https://orcid.org/0000-0002-4153-053X
Matthew Bayliss https://orcid.org/0000-0003-1074-4807
Keren Sharon https://orcid.org/0000-0002-7559-0864

## References

Abazajian, K. N., Adelman-McCarthy, J. K., Agüeros, M. A., et al. 2009, ApJS, 182, 543
Acharyya, A., Kewley, L. J., Rigby, J. R., et al. 2019, MNRAS, 488, 5862
Aggarwal, K. M., & Keenan, F. P. 1999, ApJS, 123, 311
Asplund, M., Grevesse, N., Sauval, A. J., & Scott, P. 2009, ARA&A, 47, 481
Astropy Collaboration, Robitaille, T. P., Tollerud, E. J., et al. 2013, A&A, 558, A33
Baldwin, J. A., Phillips, M. M., & Terlevich, R. 1981, PASP, 93, 5
Bayliss, M. B., Rigby, J. R., Sharon, K., et al. 2014, ApJ, 790, 144
Belfiore, F., Maiolino, R., Tremonti, C., et al. 2017, MNRAS, 469, 151
Berg, D. A., Erb, D. K., Auger, M. W., Pettini, M., & Brammer, G. B. 2018, ApJ, 859, 164
Berg, D. A., Erb, D. K., Henry, R. B. C., Skillman, E. D., & McQuinn, K. B. W. 2019, ApJ, 874, 93
Berg, D. A., Skillman, E. D., Croxall, K. V., et al. 2015, ApJ, 806, 16
Berg, D. A., Skillman, E. D., Henry, R. B. C., Erb, D. K., & Carigi, L. 2016, ApJ, 827, 126
Berg, D. A., Skillman, E. D., Marble, A. R., et al. 2012, ApJ, 754, 98
Bian, F., Fan, X., Bechtold, J., et al. 2010, ApJ, 725, 1877
Bian, F., Kewley, L. J., Dopita, M. A., & Blanc, G. A. 2017, ApJ, 834, 51
Bresolin, F. 2007, ApJ, 656, 186
Brinchmann, J., Pettini, M., & Charlot, S. 2008, MNRAS, 385, 769
Byler, N. 2018, cloudyFSPS, 1.0.0, Zenodo, doi:10.5281/zenodo.1156412
Byler, N., Dalcanton, J. J., Conroy, C., et al. 2018, ApJ, 863, 14
Byler, N., Dalcanton, J. J., Conroy, C., & Johnson, B. D. 2017, ApJ, 840, 44
Cantiello, M., Yoon, S. C., Langer, N., & Livio, M. 2007, in AIP Conf. Ser. 948, Unsolved Problems in Stellar Physics: A Conference in Honor of Douglas Gough, ed. R. J. Stancliffe et al. (Melville, NY: AIP), 413
Cardelli, J. A., Clayton, G. C., & Mathis, J. S. 1989, ApJ, 345, 245
Chisholm, J., Rigby, J. R., Bayliss, M., et al. 2019, arXiv:1905.04314, 882, 182
Choi, J., Conroy, C., & Byler, N. 2017, ApJ, 838, 159
Choi, J., Dotter, A., Conroy, C., et al. 2016, ApJ, 823, 102
Christensen, L., Laursen, P., Richard, J., et al. 2012, MNRAS, 427, 1973
Conroy, C., & Gunn, J. E. 2010, ApJ, 712, 833
Conroy, C., Gunn, J. E., & White, M. 2009, ApJ, 699, 486
Conti, P. S. 1991, ApJ, 377, 115
Crowther, P. A., Caballero-Nieves, S. M., Bostroem, K. A., et al. 2016, MNRAS, 458, 624
Crowther, P. A., Prinja, R. K., Pettini, M., & Steidel, C. C. 2006, MNRAS, 368, 895
Dopita, M. A., Sutherland, R. S., Nicholls, D. C., Kewley, L. J., & Vogt, F. P. A. 2013, ApJS, 208, 10
Dotter, A. 2016, ApJS, 222, 8
Du, X., Shapley, A. E., Martin, C. L., & Coil, A. L. 2017, ApJ, 838, 63
Eldridge, J. J., Langer, N., & Tout, C. A. 2011, MNRAS, 414, 3501
Eldridge, J. J., Stanway, E. R., Xiao, L., et al. 2017, PASA, 34, e058
Erb, D. K., Pettini, M., Shapley, A. E., et al. 2010, ApJ, 719, 1168
Erb, D. K., Shapley, A. E., Pettini, M., et al. 2006, ApJ, 644, 813
Evans, N. J., II 1999, ARA&A, 37, 311
Feltre, A., Charlot, S., & Gutkin, J. 2016, MNRAS, 456, 3354
Ferland, G. J., Porter, R. L., van Hoof, P. A. M., et al. 2013, RMxAA, 49, 137
Fitzpatrick, E. L. 1999, PASP, 111, 63
Foreman-Mackey, D., Sick, J., & Johnson, B. D. 2014, Python-fsps: Python Bindings to FSPS, 0.1.1, Zenodo, doi:10.5281/zenodo.12157
Garnett, D. R. 1992, AJ, 103, 1330
Garnett, D. R., Dufour, R. J., Peimbert, M., et al. 1995, ApJL, 449, L77
Grevesse, N., Asplund, M., Sauval, A. J., & Scott, P. 2010, Ap&SS, 328, 179
Hamann, W. R., & Gräfener, G. 2003, A&A, 410, 993
Haris, U., Parvathi, V. S., Gudennavar, S. B., et al. 2016, AJ, 151, 143
Heckman, T. M., Robert, C., Leitherer, C., Garnett, D. R., & van der Rydt, F. 1998, ApJ, 503, 646

Hillier, D. J., & Lanz, T. 2001, in ASP Conf. Ser. 247, Spectroscopic Challenges of Photoionized Plasmas, ed. G. Ferland & D. W. Savin (San Francisco, CA: ASP), 343
Hirschmann, M., Charlot, S., Feltre, A., et al. 2019, MNRAS, 487, 333
James, B. L., Aloisi, A., Heckman, T., Sohn, S. T., & Wolfe, M. A. 2014, ApJ, 795, 109
Jaskot, A. E., & Ravindranath, S. 2016, ApJ, 833, 136
Jones, A. P. 2000, JGR, 105, 10257
Kauffmann, G., Heckman, T. M., Tremonti, C., et al. 2003, MNRAS, 346, 1055
Kennicutt, R. C. J., Bresolin, F., & Garnett, D. R. 2003, ApJ, 591, 801
Kewley, L. J., & Dopita, M. A. 2002, ApJS, 142, 35
Kewley, L. J., Dopita, M. A., Leitherer, C., et al. 2013a, ApJ, 774, 100
Kewley, L. J., Dopita, M. A., Sutherland, R. S., Heisler, C. A., & Trevena, J. 2001, ApJ, 556, 121
Kewley, L. J., & Ellison, S. L. 2008, ApJ, 681, 1183
Kewley, L. J., Maier, C., Yabe, K., et al. 2013b, ApJL, 774, L10
Kewley, L. J., Nicholls, D. C., Sutherland, R., et al. 2019a, ApJ, 880, 16
Kewley, L. J., Nicholls, D. C., & Sutherland, R. S. 2019b, ARA&A, 57, 511
Kinney, A. L., Bohlin, R. C., Calzetti, D., Panagia, N., & Wyse, R. F. G. 1993, ApJS, 86, 5
Kobulnicky, H. A., & Kewley, L. J. 2004, ApJ, 617, 240
Kroupa, P. 2001, MNRAS, 322, 231
Kunth, D., & Joubert, M. 1985, A&A, 142, 411
Kurucz, R. L. 2005, MSAIS, 8, 14
Lee, H., Skillman, E. D., Cannon, J. M., et al. 2006, ApJ, 647, 970
Leitherer, C., Byler, N., Lee, J. C., & Levesque, E. M. 2018, ApJ, 865, 55
Leitherer, C., Robert, C., & Heckman, T. M. 1995, ApJS, 99, 173
Leitherer, C., Tremonti, C. A., Heckman, T. M., & Calzetti, D. 2011, AJ, 141, 37
Luridiana, V., Morisset, C., & Shaw, R. A. 2013, PyNeb: Analysis of Emission Lines, Astrophysics Source Code Library, ascl:1304.021
Maiolino, R., & Mannucci, F. 2018, arXiv:1811.09642
Mamon, G. A., Trevisan, M., Thuan, T. X., Gallazzi, A., & Davé, R. 2020, MNRAS, 492, 1791
Masters, D., McCarthy, P., Siana, B., et al. 2014, ApJ, 785, 153
McGaugh, S. S. 1991, ApJ, 380, 140
McKee, C. F., & Ostriker, J. P. 1977, ApJ, 218, 148
Mishra, A., & Li, A. 2017, ApJ, 850, 138
Nomoto, K., Kobayashi, C., & Tominaga, N. 2013, ARA&A, 51, 457
Pagel, B. E. J., Edmunds, M. G., Blackwell, D. E., Chun, M. S., & Smith, G. 1979, MNRAS, 189, 95
Pagel, B. E. J., & Tautvaisiene, G. 1995, MNRAS, 276, 505
Patrício, V., Richard, J., Carton, D., et al. 2019, MNRAS, 489, 224
Pauldrach, A. W. A., Hoffmann, T. L., & Lennon, M. 2001, A&A, 375, 161
Pauldrach, A. W. A., Kudritzki, R. P., Puls, J., & Butler, K. 1990, A&A, 228, 125
Paxton, B., Bildsten, L., Dotter, A., et al. 2011, ApJS, 192, 3
Paxton, B., Cantiello, M., Arras, P., et al. 2013, ApJS, 208, 4
Paxton, B., Marchant, P., Schwab, J., et al. 2015, ApJS, 220, 15
Peimbert, M., Peimbert, A., & Delgado-Inglada, G. 2017, PASP, 129, 082001
Pérez-Montero, E., & Amorín, R. 2017, MNRAS, 467, 1287
Pettini, M., & Pagel, B. E. J. 2004, MNRAS, 348, L59
Pettini, M., Steidel, C. C., Adelberger, K. L., Dickinson, M., & Giavalisco, M. 2000, ApJ, 528, 96
Pilyugin, L. S., & Thuan, T. X. 2005, ApJ, 631, 231
Plat, A., Charlot, S., Bruzual, G., et al. 2019, MNRAS, 490, 978
Price-Whelan, A. M., Sipőcz, B. M., Günther, H. M., et al. 2018, AJ, 156, 123
Rigby, J. R., Bayliss, M. B., Chisholm, J., et al. 2018a, ApJ, 853, 87
Rigby, J. R., Bayliss, M. B., Gladders, M. D., et al. 2014, ApJ, 790, 44
Rigby, J. R., Bayliss, M. B., Sharon, K., et al. 2018b, AJ, 155, 104
Rigby, J. R., Wuyts, E., Gladders, M. D., Sharon, K., & Becker, G. D. 2011, ApJ, 732, 59
Rivera-Thorsen, T. E., Dahle, H., Gronke, M., et al. 2017, A&A, 608, L4
Roy, A., Sutherland, R. S., Krumholz, M. R., Heger, A., & Dopita, M. A. 2019, arXiv:1907.07666
Sanders, R. L., Shapley, A. E., Kriek, M., et al. 2016, ApJ, 816, 23
Sargent, W. L. W., & Searle, L. 1970, ApJL, 162, L155
Schaerer, D., Contini, T., & Pindao, M. 1999, A&AS, 136, 35
Schaerer, D., & Vacca, W. D. 1998, ApJ, 497, 618
Schlafly, E. F., & Finkbeiner, D. P. 2011, ApJ, 737, 103
Schlegel, D. J., Finkbeiner, D. P., & Davis, M. 1998, ApJ, 500, 525
Searle, L., & Sargent, W. L. W. 1972, ApJ, 173, 25
Senchyna, P., Stark, D. P., Chevallard, J., et al. 2019, arXiv:1904.01615
Senchyna, P., Stark, D. P., Vidal-García, A., et al. 2017, MNRAS, 472, 2608
Shapley, A. E. 2011, ARA&A, 49, 525
Shapley, A. E., Steidel, C. C., Pettini, M., & Adelberger, K. L. 2003, ApJ, 588, 65
Smith, L. J., Norris, R. P. F., & Crowther, P. A. 2002, MNRAS, 337, 1309
Stark, D. P., Richard, J., Siana, B., et al. 2014, MNRAS, 445, 3200
Stasińska, G. 2005, A&A, 434, 507
Steidel, C. C., Rudie, G. C., Strom, A. L., et al. 2014, ApJ, 795, 165
Steidel, C. C., Strom, A. L., Pettini, M., et al. 2016, ApJ, 826, 159
Storey, P. J., Sochi, T., & Badnell, N. R. 2014, MNRAS, 441, 3028
Strom, A. L., Steidel, C. C., Rudie, G. C., et al. 2017, ApJ, 836, 164
Tremonti, C. A., Heckman, T. M., Kauffmann, G., et al. 2004, ApJ, 613, 898
Vidal-García, A., Charlot, S., Bruzual, G., & Hubeny, I. 2017, MNRAS, 470, 3532
Vink, J. S., & de Koter, A. 2005, A&A, 442, 587
Walborn, N. R., Fullerton, A. W., Crowther, P. A., et al. 2002, ApJS, 141, 443
Walborn, N. R., & Nichols-Bohlin, J. 1987, PASP, 99, 40
Whitaker, K. E., Rigby, J. R., Brammer, G. B., et al. 2014, ApJ, 790, 143
Wuyts, E., Rigby, J. R., Gladders, M. D., et al. 2012, ApJ, 745, 86
Wuyts, E., Rigby, J. R., Gladders, M. D., & Sharon, K. 2014, ApJ, 781, 61
Xiao, L., Stanway, E., & Eldridge, J. J. 2018, arXiv:1801.07068
Yoon, S. C., & Langer, N. 2005, A&A, 443, 643
Zahid, H. J., Dima, G. I., Kudritzki, R.-P., et al. 2014, ApJ, 791, 130
Zaritsky, D., Kennicutt, R. C. J., & Huchra, J. P. 1994, ApJ, 420, 87
Zetterlund, E., Levesque, E. M., Leitherer, C., & Danforth, C. W. 2015, ApJ, 805, 151